ASTROBIOLOGY
Volume 18, Number 5, 2018

DOI: 10.1089/ast.2017.1722

Searching for the Great Oxidation Event in North America: A Reappraisal of the Huronian Supergroup by SIMS Sulfur Four-Isotope Analysis

Huan Cui,[1,2] Kouki Kitajima,[1,2] Michael J. Spicuzza,[1,2] John H. Fournelle,[2] Akizumi Ishida,[1,2,3] Philip E. Brown,[2] and John W. Valley[1,2]

Abstract

Sedimentological observations from the Paleoproterozoic Huronian Supergroup are suggested to mark the rise in atmospheric oxygen at that time, which is commonly known as the Great Oxidation Event (GOE) and typically coupled with a transition from mass-independent fractionation (MIF) to mass-dependent fractionation (MDF) of sulfur isotopes. An early *in situ* study of S three-isotopes across the Huronian Supergroup by Papineau *et al.* (2007) identified a weak MIF–MDF transition. However, the interpretation and stratigraphic placement of this transition is ambiguous. In this study, all four S isotopes were analyzed for the first time in two Huronian drill cores by secondary ion mass spectrometer (SIMS), and both $\Delta^{33}S$ and $\Delta^{36}S$ were calculated. Based on improved precision and detailed petrography, we reinterpret the dominance of pyrrhotite in the studied sections, which was previously proposed as ''early authigenic'' in origin, as resulting from regional metamorphism. Small but analytically resolvable nonzero values of $\Delta^{33}S$ (from −0.07‰ to +0.38‰) and $\Delta^{36}S$ (from −4.1‰ to +1.0‰) persist throughout the lower Huronian Supergroup. Neither pronounced MIF-S signals nor a MIF–MDF transition are seen in this study. Four scenarios are proposed for the genesis of small nonzero $\Delta^{33}S$ and $\Delta^{36}S$ values in the Huronian: homogenization by regional metamorphism, recycling from older pyrite, dilution by magmatic fluids, and the occurrence of MDF. We argue that the precise location of the MIF–MDF transition in the Huronian remains unsolved. This putative transition may have been erased by postdepositional processes in the lower Huronian Supergroup, or may be located in the upper Huronian Supergroup. Our study highlights the importance of integrated scanning electron microscopy and secondary ion mass spectrometry techniques in deep-time studies and suggests that different analytical methods (bulk vs. SIMS) and diagenetic history (primary vs. metamorphic) among different basins may have caused inconsistent interpretations of S isotope profiles of the GOE successions at a global scale. Key Words: Great Oxidation Event (GOE)—Secondary ion mass spectrometer (SIMS)—Paleoproterozoic—Sulfur isotopes—Mass independent fractionation (MIF). Astrobiology 18, 519–538.

1. Introduction

A UNIQUE FEATURE of Earth is the existence of free oxygen in the atmosphere. However, early Earth largely lacked atmospheric oxygen for its first ~2.2 billion years (Cloud, 1972; Holland, 1978; Holland *et al.,* 1986; Farquhar *et al.,* 2011, 2014; Olson *et al.,* 2018). It is widely regarded that the rise of atmospheric oxygen on Earth has profoundly influenced the evolutionary trajectory of the atmosphere (Holland, 1978), the hydrosphere (Lyons *et al.,* 2014; Liu *et al.,* 2016), the lithosphere (Hazen *et al.,* 2008; Hazen and Ferry, 2010), and life on this planet (Cloud, 1968, 1976; Xiao, 2014; Knoll, 2015; Knoll *et al.,* 2016).

Sedimentological observations worldwide suggest that Earth witnessed the first rise in atmospheric oxygen at ~2.3 Ga, commonly known as the Great Oxidation Event (GOE) (Holland, 1984; Kasting *et al.,* 1992; Bekker *et al.,* 2004; Hannah *et al.,* 2004; Holland, 2006). This event has been widely inferred by a global sedimentological transition from the disappearance of oxygen-sensitive detrital minerals (*e.g.,* pyrite, uraninite, and siderite) and the widespread appearance of hematite-rich red beds in the sedimentary record

[1]NASA Astrobiology Institute, University of Wisconsin–Madison, Madison, Wisconsin, USA.
[2]Department of Geoscience, University of Wisconsin–Madison, Madison, Wisconsin, USA.
[3]Department of Earth Science, Tohoku University, Sendai, Japan.

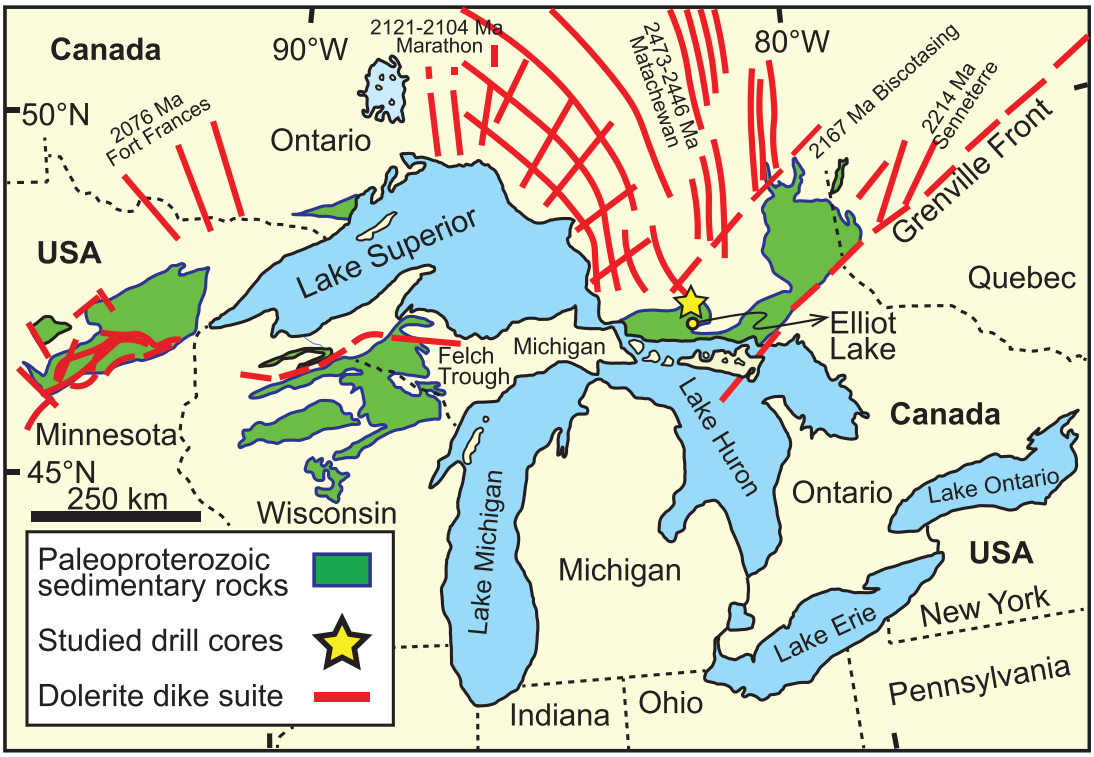

FIG. 1. Map showing the distribution of the Huronian Supergroup and other Paleoproterozoic successions in the Great Lakes area. The two studied drill cores (150–4, 156–1) are located *ca.* 10 km north of the city of Elliot Lake, Ontario, Canada. Modified from the work of Rasmussen *et al.* (2013).

(Cloud, 1968; Roscoe, 1969, 1973; Rasmussen and Buick, 1999; Dutkiewicz *et al.,* 2006; Farquhar *et al.,* 2011; Johnson *et al.,* 2014; Fischer *et al.,* 2016). Coincidently, geochemical constraints based on sulfur three-isotopes of sedimentary authigenic pyrite reveal notable disappearance of mass-independent fractionation (MIF-S) in the Paleoproterozoic, followed by over 2 billion years characterized by mass-dependent fractionation (MDF-S) (Farquhar *et al.,* 2000; Farquhar and Wing, 2003, 2005; Johnston, 2011; Ono, 2017). The discovery of the MIF–MDF transition is widely regarded as the smoking gun for the GOE (Kump, 2008).

The Huronian Supergroup in Canada (Figs. 1 and 2) is one of the most-studied Paleoproterozoic sedimentary records in the world and thus bears the potential to capture the GOE. Intensive studies have been conducted on the sedimentology (*e.g.,* Wood, 1973; Young, 1991; Hill *et al.,* 2016), geochronology (*e.g.,* Krogh *et al.,* 1984; Corfu and Andrews, 1986; Ketchum *et al.,* 2013; Rasmussen *et al.,* 2013), paleomagnetism (*e.g.,* Williams and Schmidt, 1997), biomarkers (*e.g.,* Dutkiewicz *et al.,* 2006), and chemostratigraphy (*e.g.,* Nesbitt and Young, 1982; Wing *et al.,* 2002, 2004; Bekker and Kaufman, 2007; Papineau *et al.,* 2007; Sekine *et al.,* 2011a, 2011b; Goto *et al.,* 2013) of the Huronian Supergroup.

Notably, a sulfur three-isotope study by secondary ion mass spectrometer (SIMS) was published showing mild MIF($\Delta^{33}S$) signals in rocks deposited below the Bruce diamictite (McKim and Pecors Formations) and MDF($\Delta^{33}S$) signals above the Bruce diamictite (in the Espanola Formation) (Papineau *et al.,* 2007). This tantalizing but subtle shift in the Huronian Supergroup has been used to correlate and infer the global patterns of the GOE among other Paleoproterozoic successions worldwide (*e.g.,* Papineau *et al.,* 2007; Williford *et al.,* 2011; Hoffman, 2013; Rasmussen *et al.,* 2013; Gumsley *et al.,* 2017).

However, the published $\Delta^{33}S$ data from the Huronian Supergroup all fall within a narrow range of $\Delta^{33}S = -0.25‰$ to $+0.25‰$ (*ca.* $\pm 0.23‰$, precision reported as 2SD hereafter), except three data points (0.45‰, 0.51‰, and 0.88‰) that have been interpreted as critical MIF-S signals marking the end of the GOE (Papineau *et al.,* 2007). The absence of a stronger MIF–MDF transition in the Huronian stands in strong contrast to other GOE sections where $\Delta^{33}S$ values are up to $+7‰$ (Guo *et al.,* 2009; Luo *et al.,* 2016) and suggested the need for a more comprehensive study including $\Delta^{36}S$ analysis.

Questions based on the published $\Delta^{33}S$ record in Huronian sediments include the interpretation of faint MIF and MDF signals and thereby the location of MIF–MDF transition and of the GOE. (1) Might the small nonzero $\Delta^{33}S$ values be an artifact of poorer analytical precision in early studies? (2) If real, are the small nonzero $\Delta^{33}S$ values due to MIF? Alternatively, these small MIF signals might reflect remobilized compositions from an older MIF-bearing sulfur reservoir (*e.g.,* Ulrich *et al.,* 2011; Williford *et al.,* 2011; Cabral *et al.,* 2013; Reinhard *et al.,* 2013), a period with diminished photochemical reaction in the atmospheric S cycle (Williford *et al.,* 2011), or some other conditions that favor the production of a prolonged, muted $\Delta^{33}S$ signature (*e.g.,* Thomazo *et al.,* 2009). (3) Does the weak MIF–MDF transition in the lower Huronian (Papineau *et al.,* 2007) reflect variation in secular S isotope signals or values altered by regional metamorphism? It should be taken as cautionary

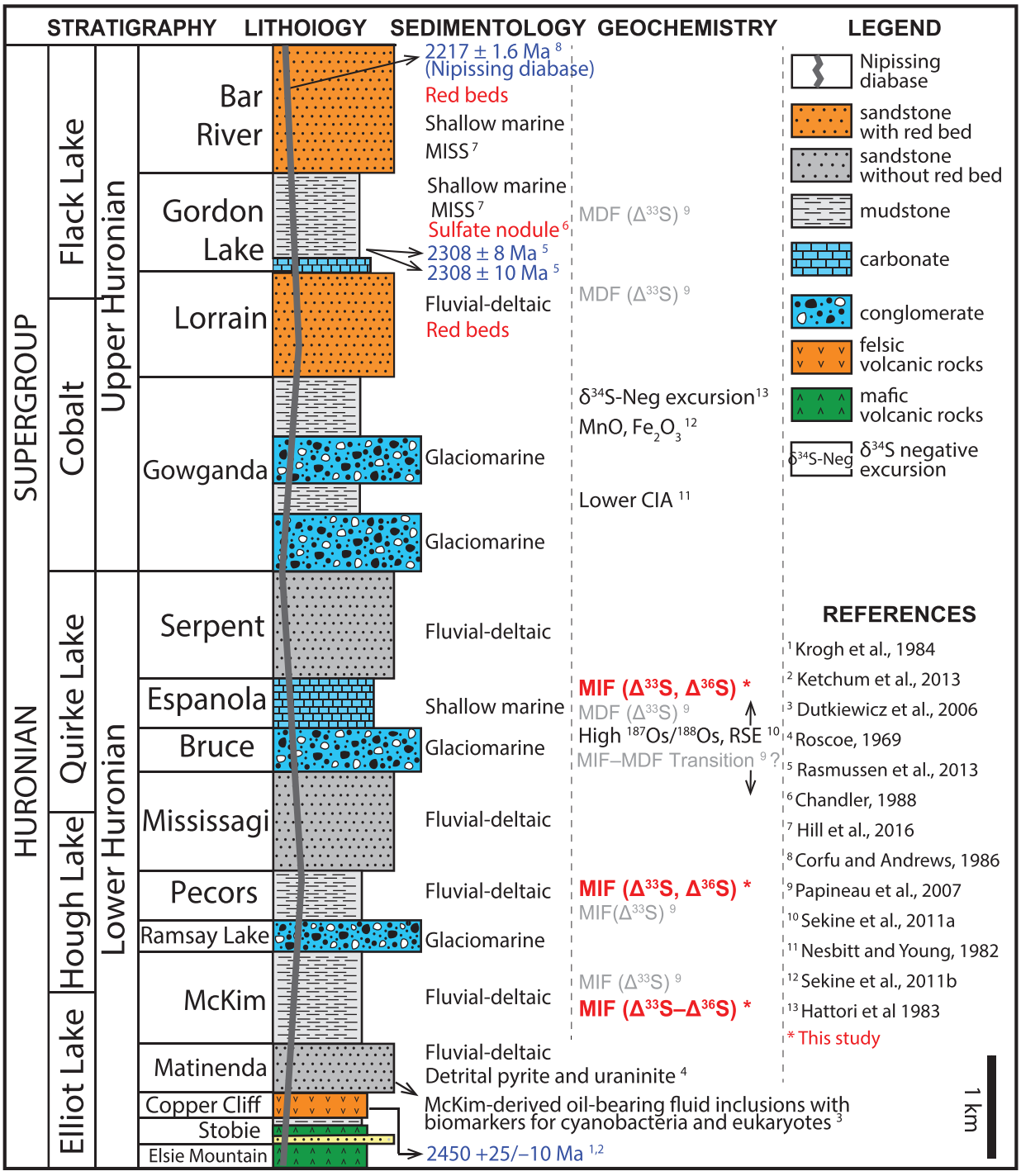

FIG. 2. Integrated lithostratigraphy, sedimentology, and geochemical studies of the Huronian Supergroup. Lithostratigraphy modified after Young *et al.* (2001), Dutkiewicz *et al.* (2006), and Hill *et al.* (2016). Sedimentological observations include detrital pyrite and uraninite (Roscoe, 1969), oil-bearing fluid inclusions (Dutkiewicz *et al.*, 2006), red beds (Roscoe, 1973), microbially induced sedimentary structures (Hill *et al.*, 2016), and sulfate nodules (Chandler, 1988). Age constraints were measured from Nipissing diabase (Corfu and Andrews, 1986) and Copper Cliff Formation (Krogh *et al.*, 1984; Ketchum *et al.*, 2013). Geochemical data include sulfur isotopes (Hattori *et al.*, 1983; Papineau *et al.*, 2007), CIA (Nesbitt and Young, 1982), high initial $^{187}Os/^{188}Os$ and redox-sensitive elements (*e.g.*, Mo, Re) (Sekine *et al.*, 2011a), and $MnO–Fe_2O_3$ enrichment right after the Gowganda glaciation (Sekine *et al.*, 2011b). Note that the previously proposed MIF–MDF transition (Papineau *et al.*, 2007) has been reevaluated in this study. Abbreviations: CIA = chemical index of alteration; MDF = mass-dependent fractionation; MIF = mass-independent fractionation; MISS = microbially induced sedimentary structure; RSE = redox-sensitive elements.

that most published Huronian $\Delta^{33}S$ data points can hardly be distinguished between MIF and MDF.

To answer these questions, we conducted a SEM–SIMS study that combines petrography and imaging with *in situ* S four-isotope study of the Huronian sulfide minerals by SIMS. Improved analytical precision of all four S isotopes was achieved with modifications of the SIMS detector system and analytical protocols (Ushikubo *et al.,* 2014). Both $\Delta^{33}S$ and $\Delta^{36}S$ were determined for the first time by SIMS in the Huronian. Two of the previously studied drill cores of the Huronian Supergroup were analyzed to reevaluate the dynamics of biogeochemical S cycles and atmospheric oxygen evolution in this critical period.

2. Geological Background

The Huronian Supergroup is comprised of five groups: Elliot Lake, Hough Lake, Quirke Lake, Cobalt, and Flack Lake, in ascending stratigraphic order (Fig. 2). There are three distinct glacial diamictite deposits: Ramsay Lake, Bruce, and Gowganda Formations (Roscoe, 1969; Wood, 1973; Young, 1991, 2002; Melezhik *et al.,* 2013).

The lower Huronian Supergroup includes basal detrital and volcanic rocks and the lower two suites of diamictite. The Matinenda Formation is deposited on an Archean unconformity surface and contains detrital pyrite (FeS_2) and uraninite (UO_2) in sandstones and conglomerates, which have been widely accepted as evidence for anoxic conditions during sediment transportation and deposition (Roscoe, 1969; Zhou *et al.,* 2017). In addition, organic geochemistry studies on oil-bearing fluid inclusions in quartz of the Matinenda suggest hydrocarbons are derived from the overlying McKim Formation (Dutkiewicz *et al.,* 2006). Going up section, the McKim and Pecors Formations straddle the Ramsay Lake diamictite and are both fluvial-deltaic facies mudstones. Above the Bruce diamictite, the Espanola Formation shows bedded carbonates likely deposited in a shallow marine environment.

The upper Huronian Supergroup starts with the glacial Gowganda diamictites. Above the uppermost Gowganda diamictite, hematite-rich red beds are found in the Lorrain Formation, the first appearance of oxidized sediments in this region and widely regarded as a sedimentological response to an oxidizing atmosphere (Roscoe, 1973). Sulfate nodules were found in the Gordon Lake Formation (Chandler, 1988), further suggesting the onset of oxidative weathering of pyrite. Red granitic clasts in the Gowganda tillites are frequently interpreted as the result of post-GOE weathering, but the timing of oxidative alteration is uncertain. Abundant microbially induced sedimentary structures have been identified in the Gordon Lake Formation and the overlying Bar River Formation, suggesting microbial colonization during deposition (Hill *et al.,* 2016).

Geochronological constraints for the Huronian Supergroup include radiometric ages of zircons from the felsic volcanic rocks in the Copper Cliff Formation near the base of the supergroup (*ca.* 2.45 Ga) (Krogh *et al.,* 1984; Ketchum *et al.,* 2013) and U–Pb zircon ages (*ca.* 2.3 Ga) in the Gordon Lake Formation (Rasmussen *et al.,* 2013). Concordant baddeleyite and rutile ages from the Nipissing diabase toward the top of this supergroup (*ca.* 2.22 Ga) provide a younger age constraint, consistent with zircon ages (Corfu and Andrews, 1986) (Fig. 2).

The maximum metamorphic grade for the Huronian Supergroup at the studied locations is lower greenschist facies (350°C), which probably occurred either during the Penokean orogeny (~1.89–1.8 Ga) (Card, 1978; Young *et al.,* 2001) or during the intrusion of the Nipissing diabase dike swarm at *ca.* 2.22 Ga (Mossman *et al.,* 1993).

3. Materials and Methods

3.1. Sampling strategy

In this study, to help avoid detrital components, only marine facies (*i.e.,* carbonate- or siltstone-dominated intervals) were selected for petrographic and geochemical analysis. The sampled intervals include the McKim Formation (marine siltstone), the Pecors Formation (marine siltstone), and the Espanola Formation (marine siltstone and limestone). Due to the large contribution by detrital/terrestrial sediments in siliciclastic facies (*e.g.,* Ulrich *et al.,* 2011; Zhou *et al.,* 2017), the sandstone-dominated Mississagi and Serpent formations and the three diamictite intervals were avoided during sampling. A suite of 16 samples from two Huronian drill cores was analyzed for S four-isotopes by SIMS, including 11 samples from the Kerr-McGee drill core 150–4 (Supplement S2; Supplementary Data are available at http://online.liebertpub.com/doi/suppl/10.1089/ast.2017.1722) and 5 samples from the Kerr-McGee drill core 156–1 (Supplement S3). Based on the Ontario Geological Survey map #2419, these two cores are located *ca.* 10 km north of the city of Elliot Lake, Ontario, Canada (Fig. 1; Fig. 1 in Papineau *et al.,* 2007). All the drill core samples are stored in the Ontario Geological Survey Repository at Sault Ste. Marie, Canada.

Several sulfide minerals have been found in the Huronian samples, which include pyrite, pyrrhotite, chalcopyrite, sphalerite, pentlandite, and cobaltite. Due to ''orientation effects'' that degrade accuracy for SIMS data in a few minerals (Kozdon *et al.,* 2010; Kita *et al.,* 2011), sphalerite was not considered for analysis in this study. Only grains of pyrite, pyrrhotite, and chalcopyrite, that have been shown not to have orientation effects, were analyzed by SIMS for S four-isotopes in this study. Most of the sulfide minerals are anhedral in shape, showing irregular morphology commonly intergrowing with chlorite and other silicate minerals (Fig. 3). SIMS samples were cast in round mounts with the UWPy-1 pyrite standard near the center of the 25 mm diameter, 5 mm thick mount. All analyzed minerals were imaged by scanning electron microscope (SEM) with back-scattered electrons (BSE) prior to SIMS analysis. Mineral chemistry was verified by SEM energy-dispersive spectrometry (EDS) and wavelength-dispersive electron-probe microanalysis (EPMA).

3.2. SIMS analysis

Sulfur four-isotope data were measured with a CAMECA IMS 1280 in the WiscSIMS (Wisconsin Secondary Ion Mass Spectrometer) Lab at the University of Wisconsin–Madison. Detailed methods can be found in previous publications (Valley and Kita, 2009; Kozdon *et al.,* 2010; Williford *et al.,* 2011, 2016; Ushikubo *et al.,* 2014) and are only briefly described below.

Analysis of sulfur four-isotopes employed a $^{133}Cs^+$ beam (~5 nA) accelerated at 10 kV (impact energy = 20 kV). The beam size in this study is 20 μm. Samples were coated with

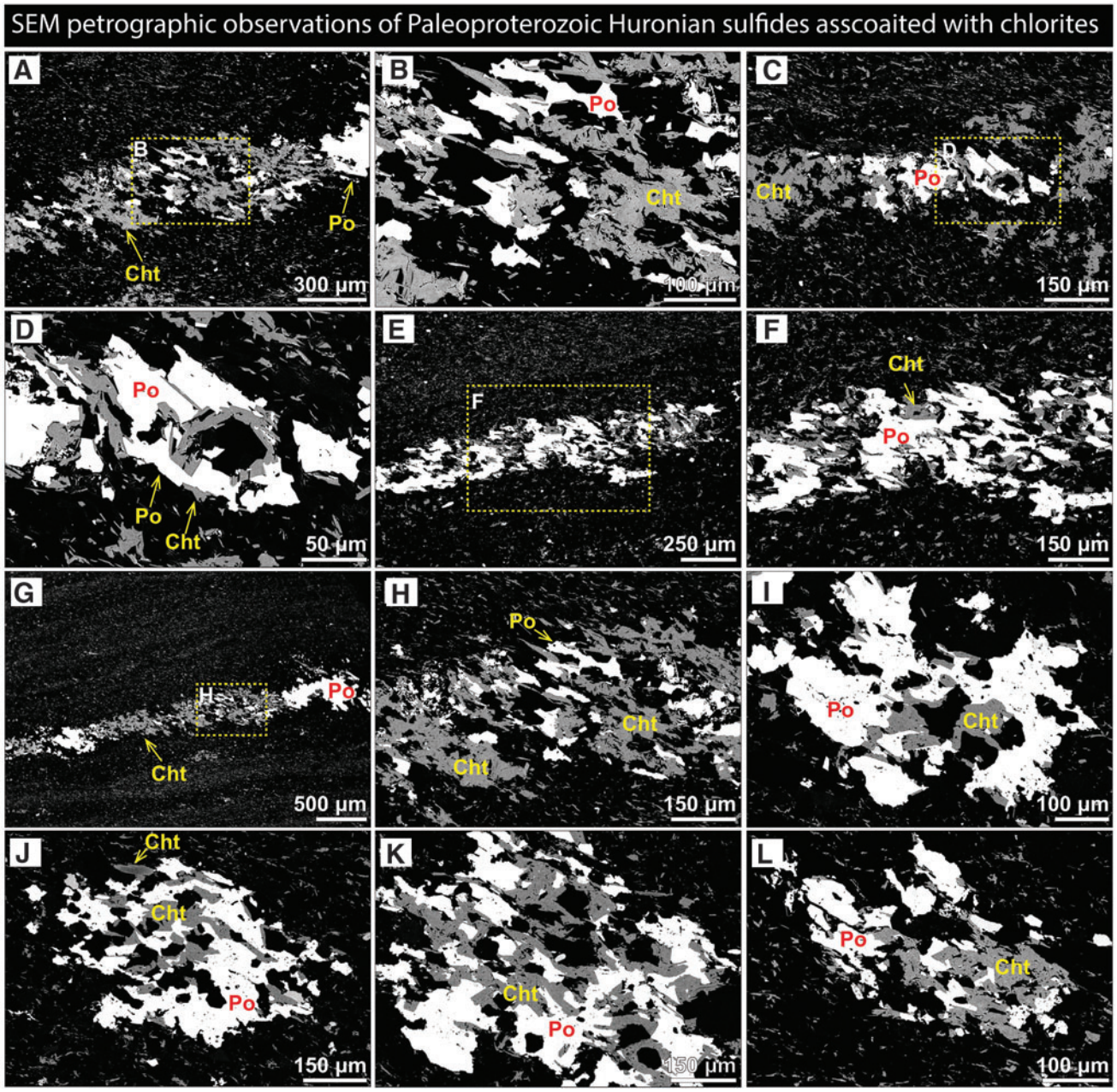

FIG. 3. Back-scattered electron (BSE) images of the Huronian samples show close association between pyrrhotite (Po) and chlorite (Cht). Images B, D, F, H show the marked zones in images A, C, E, G, respectively. Sample depth: (**A**–**D**) 4625.1 m in drill core 156–1; (**E**, **F**) 4559 m in drill core 156–1; (**G**, **H**) 4625.1 m in drill core 156–1; (**I**–**L**) 5219 m in drill core 150–4.

60 nm of gold, and a normal-incidence electron flood gun was used for charge compensation. Secondary ions of $^{32}S^-$, $^{33}S^-$, $^{34}S^-$, and $^{36}S^-$ were detected simultaneously using four Faraday cup detectors with modified slits as described by Ushikubo *et al.* (2014). UWPy-1 (pyrite) was used as running standard with $\delta^{34}S = 16.04 \pm 0.18‰$ CDT, $\Delta^{33}S = -0.003 \pm 0.009‰$, and $\Delta^{36}S = -0.21 \pm 0.24‰$ values analyzed by conventional gas source mass spectrometer (Ushikubo *et al.,* 2014; Williford *et al.,* 2016). The running standard is mounted in the center of each SIMS sample mount together with the unknown Huronian samples in order to closely monitor the running conditions during SIMS analysis. The raw isotope ratios were corrected for instrumental bias using mineral-specific lab standards: UWPy-1, Anderson pyrrhotite, and Trout Lake chalcopyrite (Crowe and Vaughan, 1996; Kozdon *et al.,* 2010) (Supplement S1). Analytical spot-to-spot precisions are $\delta^{34}S \pm 0.39‰$, $\Delta^{33}S \pm 0.04‰$, and $\Delta^{36}S \pm 1.13‰$ (2SD) based on the groups of eight bracketing UWPy-1 standard analyses during the SIMS session of Huronian samples (Supplement S4), which is comparable to what Ushikubo *et al.* (2014) reported in previous sessions ($\delta^{34}S \pm 0.23‰$, $\Delta^{33}S \pm 0.05‰$, $\Delta^{36}S \pm 0.86‰$). UWPy-1 was analyzed a total of 157 times in this study (Supplement S4).

Each analysis consisted of 10 s for pre-sputtering, 80 s for centering of secondary ions in the field aperture, and 80 s for isotope measurement. Average count rates for $^{32}S^-$ confirmed the stability of individual analyses. A typical count rate of $^{32}S^-$ was $\sim 5\times10^9$ counts per second for pyrrhotite and pyrite, and $\sim 6\times10^9$ counts per second for chalcopyrite. To monitor the magnitude of interference from $^{32}SH^-$ on the $^{33}S^-$ signal, the $^{32}SH^-$ peak was measured by scanning the deflector located between the magnet and the Faraday cup detectors after each analysis (Williford *et al.,* 2011). The ratio of the $^{32}SH^-$ tail at the $^{33}S^-$ peak position relative to the $^{32}SH^-$ peak ($^{32}SH^-_{tail}/^{32}SH^-_{peak}$) was determined to be $\sim 1\times10^{-5}$, which was used to correct the contribution of the $^{32}SH^-$ tail signal to the $^{33}S^-$ peak. The contribution of $^{32}SH^-$ to the $^{33}S^-$ peak in all the spots is negligible (with corrections from 0.0001‰ to 0.001‰).

After SIMS analysis, gold coating of the samples was removed by chemical dissolution of gold with saturated aqueous solution of potassium iodide (Jones *et al.,* 2012). Samples were recoated with 20 nm thickness of carbon, and each pit was investigated by SEM-SE for possible irregularities.

3.3. Sulfur four-isotope data correction

Sulfur isotope ratios are reported in standard per mil (‰) notation relative to Vienna Canyon Diablo Troilite (VCDT). Measured ratios of $^{34}S/^{32}S$, $^{33}S/^{32}S$, and $^{36}S/^{32}S$ were divided by VCDT values and calculated as "raw" δ-values: $\delta^{34}S_{raw}$, $\delta^{33}S_{raw}$, and $\delta^{36}S_{raw}$, respectively. The sulfur isotope ratios of VCDT used in the calculations are $^{34}S/^{32}S = 1/22.6436$, $^{33}S/^{32}S = 1/126.948$ (Ding *et al.,* 2001), and a revised $^{36}S/^{32}S$ value of 1/6641 (Ushikubo *et al.,* 2014) instead of 1/6515 (Ding *et al.,* 2001). Correction for $^{32}SH^-$ contribution to the $^{33}S^-$ peak was applied at this step. In this study, UWPy-1 (Balmat pyrite) was used as the monitoring standard for all the samples.

Correction factors of the instrumental bias of $\delta^{34}S$ for pyrite samples are calculated based on the S four-isotope values of UWPy-1 measured by conversion of powdered sample to SF_6 and gas-source mass spectrometry (Ushikubo *et al.,* 2014). Although only the UWPy-1 pyrite standard was mounted in the center of each SIMS sample, pyrrhotite and chalcopyrite standards in other standard mounts were also analyzed at the beginning of each session in order to constrain the instrumental bias between different sulfide minerals (Supplement S1). In addition, Rutan pyrite and Norilsk chalcopyrite were run as checks for accuracy. Relative bias between pyrrhotite and pyrite was calculated based on the offset between UWPy-1 pyrite standard and Anderson pyrrhotite standard. All the corrected data, together with the corresponding petrographic images by SEM, can be found in the online supplementary materials (Supplements S1–S4).

3.4. EPMA analysis

Major element concentrations of sulfide minerals, including pyrrhotite, chalcopyrite, sphalerite, pentlandite, pyrite, and cobaltite, were analyzed by EPMA for Fe, S, Co, Ni, Cu, Zn, and As concentrations using wavelength-dispersive crystal spectrometers. Before EPMA, each spot was investigated by SEM, BSE, and EDS. EPMA was performed with a CAMECA SXFive FE electron microprobe at 20 kV, 20 nA and 1 micron defocused beam, with Astimex sulfide as well as pure metal standards, using the Armstrong/Love-Scott matrix correction, with Probe for Windows software (Donovan *et al.,* 2018) at the Eugene Cameron Electron Microprobe Lab, Department of Geoscience, University of Wisconsin–Madison.

4. Results

4.1. Petrographic observations

Detailed petrographic investigation reveals multiple sulfide minerals, including pyrite, pyrrhotite, chalcopyrite, pentlandite, sphalerite, and cobaltite in the studied samples (Figs. 3–8; see Supplements S2–S4 for a complete log of isotope sample and standard analyses). EPMA data (Supplement S5) confirm the identification of these minerals.

Compared with other roughly time-equivalent strata that have been studied for S three- or four-isotopes (Guo *et al.,* 2009; Williford *et al.,* 2011; Luo *et al.,* 2016), a distinct feature of the Huronian samples is the dominance of pyrrhotite as the main sulfide mineral. Both granular and elongated grains of pyrrhotite and subordinate pyrite were imaged and analyzed for multiple S isotopes. Elongate grains are typically aligned parallel to foliation and intergrown with chlorite (Fig. 3). Most of the pyrrhotite grains have fine pentlandite intergrowths or exsolution (Fig. 6). Cobaltite is also seen in a few samples; grains are mostly euhedral and cutting across the pyrrhotite (Fig. 8), suggesting a relatively late-stage mineralization.

4.2. SIMS S four-isotope results

Chemostratigraphic profiles of the Huronian Supergroup in Fig. 9 present all the new data measured by SIMS in this study. The $\delta^{34}S$ profiles of both drill cores show mostly positive values from 0‰ to +5‰, except for a few slightly negative values in the McKim Formation of drill core 150–4 (Fig. 9A), and notably positive $\delta^{34}S$ data of *ca.* +15‰ in chalcopyrite of the Espanola Formation of the drill core 156–1 (Fig. 9D). In drill core 150–4, $\Delta^{33}S$ values of this study range from +0.004‰ to +0.38‰ (Fig. 9B), while in drill core 156–1, the $\Delta^{33}S$ data range from −0.07‰ to +0.26‰ (Fig. 9E) (average 2SD = ±0.04‰ for an individual analysis). Compared with the earlier study (Papineau *et al.,* 2007), we also simultaneously analyzed $\Delta^{36}S$. New $\Delta^{36}S$ values analyzed from the same Huronian samples range from −4.1‰ to +1.0‰ in drill core 150–4 (Fig. 9C) and from −3.6‰ to +0.5‰ in drill core 156–1 (Fig. 9F) (average 2SD = ±1.13‰ for an individual analysis).

Cross-plots of $\delta^{34}S$ versus $\Delta^{33}S$ and $\Delta^{33}S$ versus $\Delta^{36}S$ are tightly clustered and do not show clear correlations or $\Delta^{36}S$ versus $\Delta^{33}S$ slopes (Fig. 10). Values of $\delta^{34}S$ from pyrrhotite and chalcopyrite are generally higher than pyrite in both drill cores 150–4 and 156–1. These $\delta^{34}S$ fractionations are reversed and do not represent equilibration during deposition or metamorphism (Ohmoto and Rye, 1979; Ohmoto, 1986; Seal, 2006). Chalcopyrite grains reveal the most positive $\delta^{34}S$ values among all sulfides.

To assess the published and new $\Delta^{33}S$ data sets, a close evaluation of the point-to-point precision is necessary. It should be noted that the published uncertainties for the $\Delta^{33}S$ data by Papineau *et al.* (2005) are an integration of both internal error and external error calculated using a York-based regression technique (Papineau *et al.,* 2005,

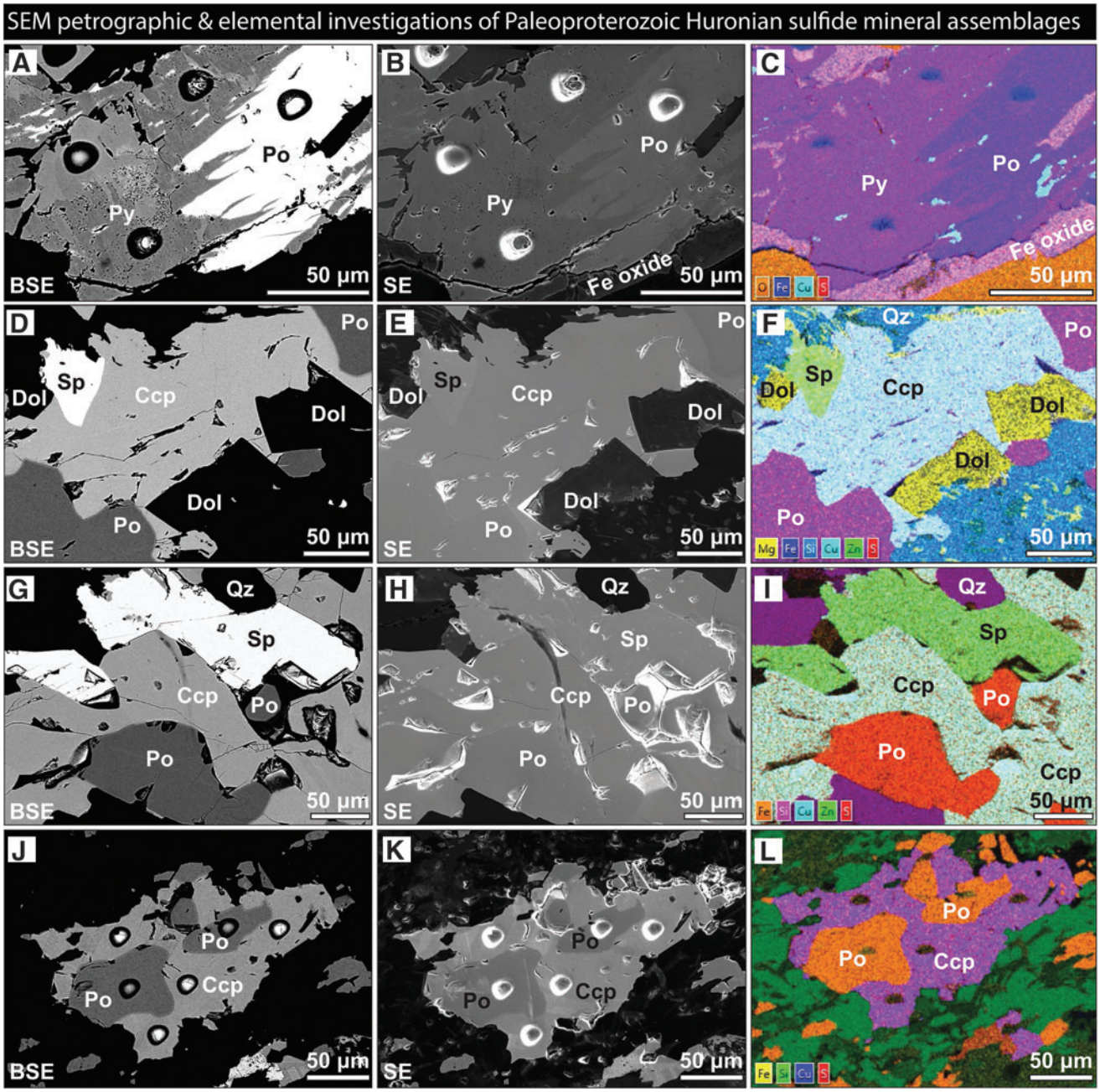

FIG. 4. Petrographic observations and elemental mapping of multiple sulfide minerals coexisting in the same view. (**A–C**) Pyrite and pyrrhotite; (**D–F**) pyrrhotite, chalcopyrite, and sphalerite; (**G–I**) pyrrhotite, chalcopyrite, and sphalerite; (**J–L**) pyrrhotite and chalcopyrite. Sample depth: (A) 4638 m in drill core 156–1; (B, C) 4625.1 m in drill core 156–1; (D) 4490 m in drill core 156–1. Abbreviations: Ccp = chalcopyrite; Dol = dolomite; Po = pyrrhotite; Py = pyrite; Qz = quartz; Sp = sphalerite.

2007), while the reported 2SD of SIMS data in our study is the measured reproducibility of the bracketing UWPy-1 standard that were measured throughout our analysis sessions ($n = 157$) (Supplement S4). Thus a direct comparison of the published precisions of these two data sets may be misleading. Therefore, we have made a direct comparison of the reproducibility of analyzed sulfur isotope data for homogeneous standard material (Balmat pyrite, UWPy-1) in both data sets. The 2SD values calculated from repeated analyses of the UWPy-1 standard ($n = 157$) in this study are ±0.39‰ ($\delta^{34}S$), ±0.04‰ ($\Delta^{33}S$), and ±1.13‰ ($\Delta^{36}S$). The 2SD values of $\delta^{34}S$ and $\Delta^{33}S$ data are systematically 2–3 times smaller than the ones calculated from a Balmat pyrite standard (not UWPy-1, $n = 11$) in the work of Papineau *et al.* (2005) that show precisions of ±0.69‰ ($\delta^{34}S$), ±0.14‰ ($\Delta^{33}S$).

5. Discussion

5.1. Origin of the pyrrhotite in the Huronian

A distinct feature of the studied intervals in the Huronian Supergroup is the dominance of pyrrhotite among all sulfide minerals. This is in strong contrast with other roughly equivalent Paleoproterozoic successions with pyrite as the

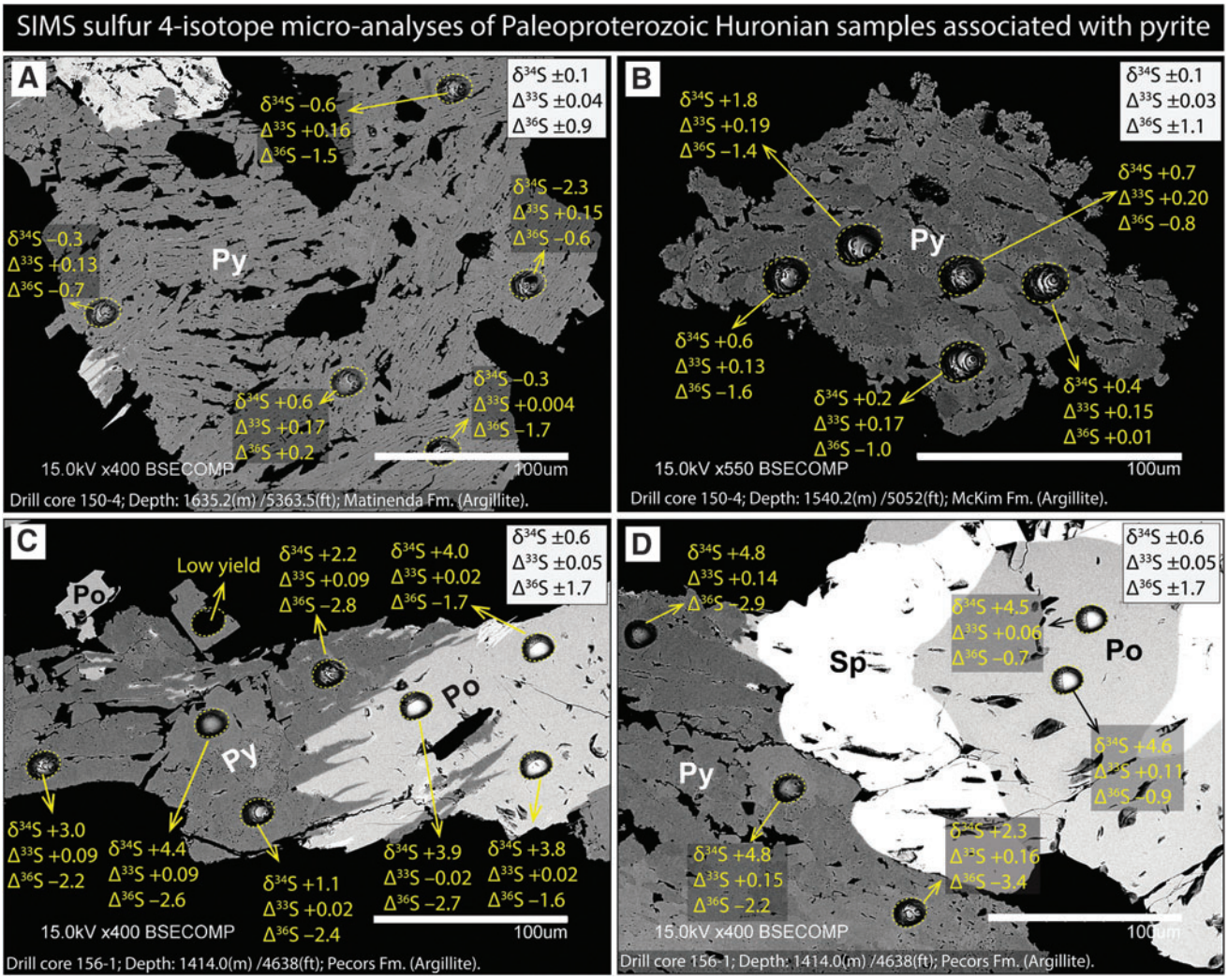

FIG. 5. Back-scattered electron (BSE) images with SIMS sulfur isotope data of representative pyrite from the Kerr–McGee drill cores 150–4 and 156–1 of the Huronian Supergroup. Silicate matrix is black. Abbreviations: Po = pyrrhotite; Py = pyrite; Sp = sphalerite. The upper right of each figure shows precisions of $\delta^{34}S$, $\Delta^{33}S$, and $\Delta^{36}S$ with two standard deviations. All data can be found in the online supplementary material.

dominant sulfide mineral (*e.g.,* Guo *et al.,* 2009; Williford *et al.,* 2011; Luo *et al.,* 2016). Therefore, interpretation of S isotope profiles of the Huronian Supergroup requires understanding on the genesis of the Huronian pyrrhotite.

Pyrrhotite has been reported from both ancient strata (Reynolds *et al.,* 1990; Reuschel *et al.,* 2012; Asael *et al.,* 2013; Minguez *et al.,* 2016) and modern marine sediments (Horng and Roberts, 2006; Larrasoaña *et al.,* 2007; Kars and Kodama, 2015; Honsho *et al.,* 2016). However, pyrrhotite is rare in modern marine sediments and is often detrital in origin resulting from rapid weathering and short distances of transport (Horng and Roberts, 2006). In other cases, pyrrhotite has been found associated with gas hydrates (Kars and Kodama, 2015) or hydrocarbon seepage (Reynolds *et al.,* 1990). Pyrrhotite has also been reported in ancient sedimentary records such as the *ca.* 2.0 Ga Pilgujärvi Sedimentary Formation in northwest Russia (Reuschel *et al.,* 2012) and *ca.* 2.0 Ga Zaonega Formation in Karelia (Asael *et al.,* 2013), which have both been interpreted to result from the decomposition of pyrite during low-grade metamorphism.

Previously, pyrrhotite in the Huronian was interpreted as *early* authigenic (Papineau *et al.,* 2007). Based on this interpretation, the measured S isotope values from these pyrrhotites have been used to infer secular variation in atmospheric oxygen and marine sulfur cycle (Papineau *et al.,* 2007) and global correlations of the GOE-bearing sections (Hoffman, 2013; Gumsley *et al.,* 2017).

However, in this study, multiple lines of evidence suggest that pyrrhotite in the studied samples actually formed during regional metamorphism. The evidence includes

(1) *Irregular/anhedral shape and large grain size.* Most of the pyrrhotite grains show irregular/anhedral shapes, remarkably large (up to several hundred micrometers) in size (Figs. 3–8; Supplements S2 and S3), which look unlikely to be formed in a water column or shallow marine sediment.

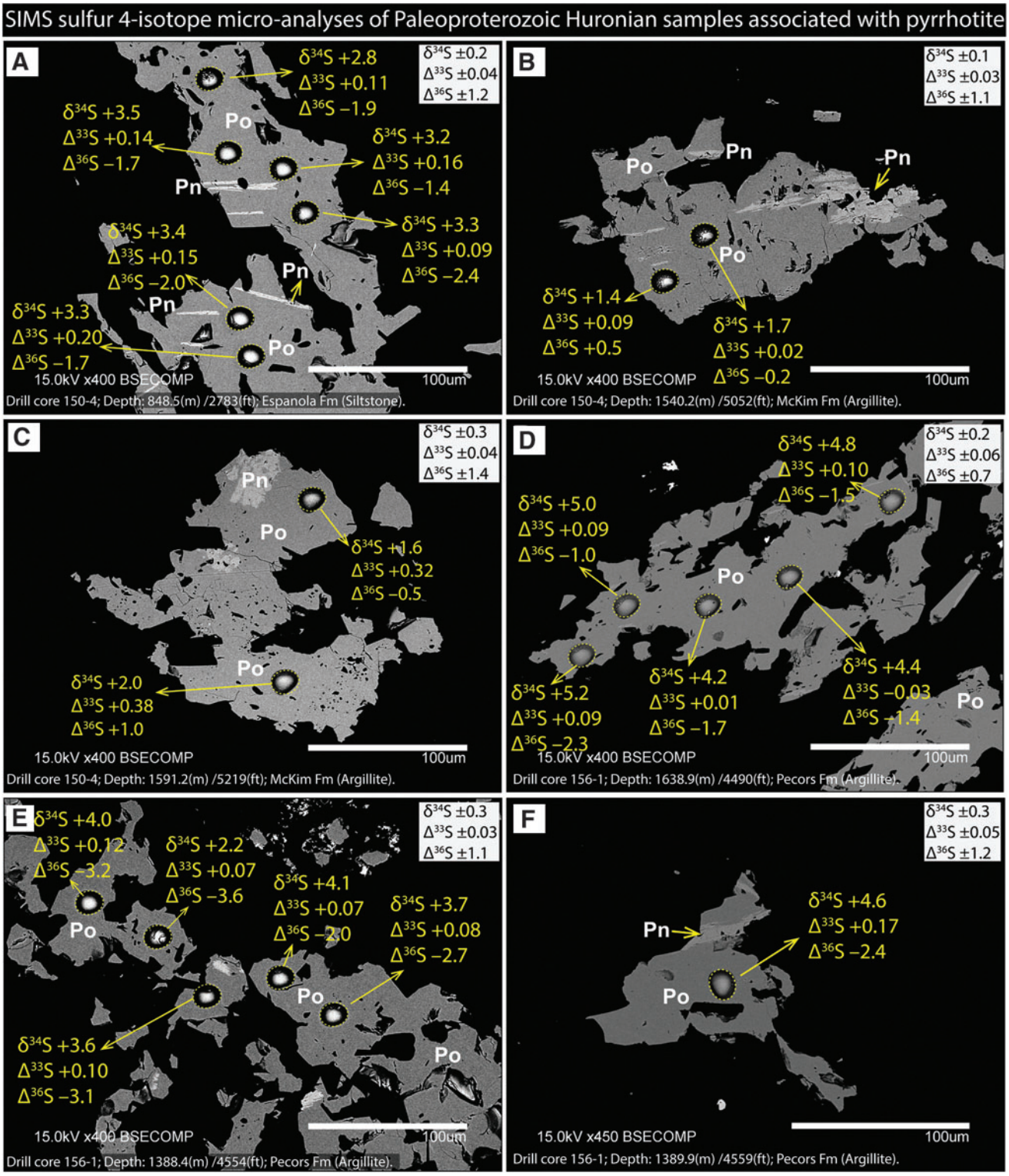

FIG. 6. Back-scattered electron (BSE) images with SIMS sulfur isotope data of representative pyrrhotite from the Kerr–McGee drill cores 150–4 and 156–1 of the Huronian Supergroup. Silicate matrix is black. Abbreviations: Pn = pentlandite; Po = pyrrhotite. The upper right of each figure shows precisions of $\delta^{34}S$, $\Delta^{33}S$, and $\Delta^{36}S$ with two standard deviations. All data can be found in the online supplementary material.

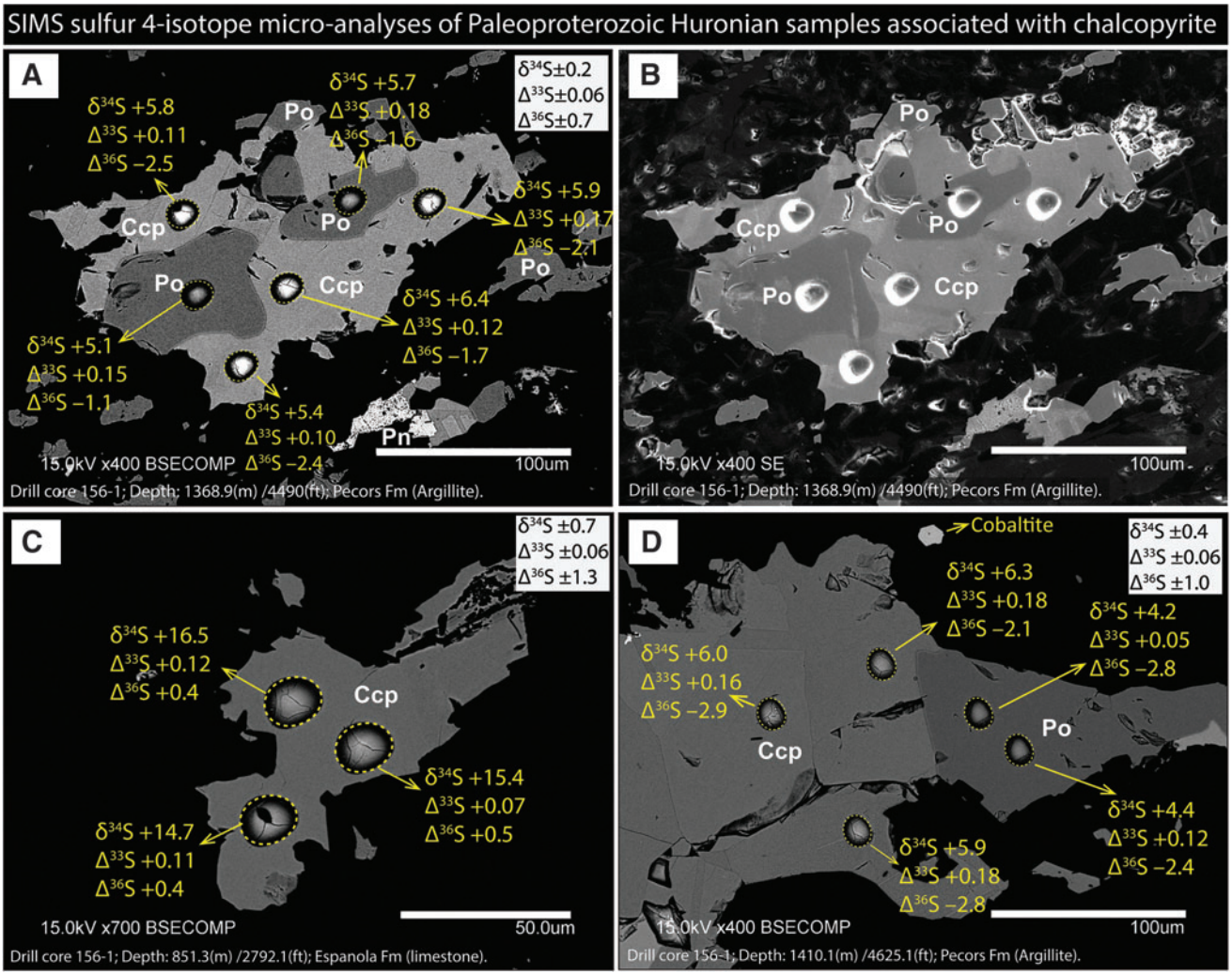

FIG. 7. Back-scattered electron (BSE) and secondary electron (SE, in B) images with SIMS data of representative chalcopyrite from the Kerr–McGee drill cores 150–4 and 156–1 of the Huronian Supergroup. Silicate matrix is black. Abbreviations: Ccp = chalcopyrite; Pn = pentlandite; Po = pyrrhotite. The upper right of each figure shows precisions of $\delta^{34}S$, $\Delta^{33}S$, and $\Delta^{36}S$ with two standard deviations. All data can be found in the online supplementary material.

(2) *Diverse mineral assemblages*. We found that many pyrrhotite grains are parallel with metamorphic foliation and intimately associated with chlorite, pentlandite, and chalcopyrite (Figs. 3 and 4; Supplements S2 and S3), which suggest metamorphism.

(3) *Homogeneous compositions*. All the studied pyrrhotites have remarkably homogeneous compositions of sulfur isotope ratios and elemental abundances at micrometer scales (Figs. 5–9; Supplements S2 and S3), which is in contrast with early marine sulfides that typically show strong heterogeneity in composition due to a biogenic nature of microbial sulfate reduction (Kohn *et al.,* 1998; McLoughlin *et al.,* 2012; Wacey *et al.,* 2015; Simpson *et al.,* 2017) and Rayleigh distillation in restricted pore-water environments (*e.g.,* Ferrini *et al.,* 2010; Williford *et al.,* 2011; Fischer *et al.,* 2014; Zhelezinskaia *et al.,* 2014; Lin *et al.,* 2016; Magnall *et al.,* 2016). The above observations suggest that the Huronian pyrrhotites formed post-deposition, likely during low-grade regional metamorphism.

5.2. Reevaluating the "MIF–MDF transition" in the Huronian

The sedimentological transition in the Huronian reveals the existence of detrital pyrite and uraninite in the lower Huronian and of red beds in the upper Huronian, which has been widely accepted to bracket the rise in atmospheric oxygen (Roscoe, 1969, 1973). If correct, one would expect to see a corresponding MIF–MDF transition in both $\Delta^{33}S$ and $\Delta^{36}S$ profiles of the Huronian Supergroup. The MIF–MDF transition has been proposed based on small MIF($\Delta^{33}S$) signals that were interpreted to exist in strata below the Bruce diamictite versus MDF($\Delta^{33}S$) signals in the Espanola carbonates above the Bruce diamictite (Papineau *et al.,* 2007) (Fig. 11D, 11H).

However, the new $\Delta^{33}S$ data with improved precision suggest a different view. Our $\Delta^{33}S$ data all fall within a very

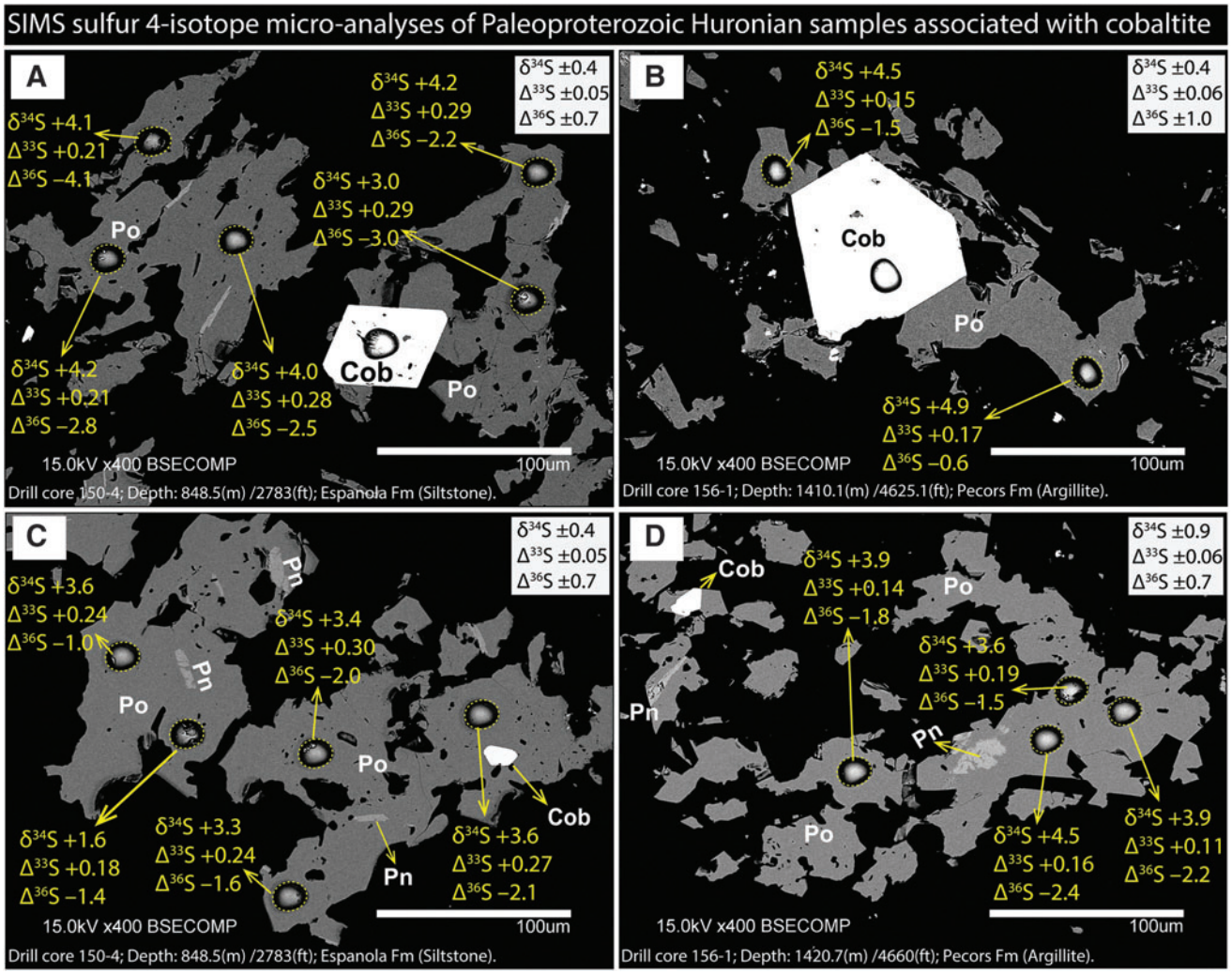

FIG. 8. Back-scattered electron (BSE) images of representative cobaltite. S isotope data are not provided for the cobaltite due to the lack of SIMS standards. Silicate matrix is black. Abbreviations: Cob = cobaltite; Pn = pentlandite; Po = pyrrhotite. The upper right of each figure shows precisions of $\delta^{34}S$, $\Delta^{33}S$, and $\Delta^{36}S$ with two standard deviations. All data can be found in the online supplementary material.

narrow range. Small nonzero $\Delta^{33}S$ values persist throughout the lower Huronian including the Espanola. *Neither pronounced MIF-S signals nor a MIF–MDF transition are seen in this study* (Fig. 11C, 11G).

The newly analyzed $\Delta^{36}S$ data further show nonzero signals in the lower Huronian. In contrast with the proposed ''MDF-S'' interval for the Espanola Formation that is based on $\Delta^{33}S$ data (Papineau *et al.,* 2007), the $\Delta^{36}S$ data analyzed from the same Huronian samples range from –4.1‰ to +1.0‰ in drill core 150–4 (Fig. 9C) and from –3.6‰ to +0.5‰ in drill core 156–1 (Fig. 9F), which show that nonzero $\Delta^{36}S$ signals also persist throughout the lower Huronian, including the Espanola.

In summary, although the entire studied interval in the lower Huronian shows a narrow range, the nonzero $\Delta^{33}S$ and $\Delta^{36}S$ signals are still distinguishable. These small but analytically resolvable nonzero signals exist before and after both glaciations of the lower Huronian Supergroup and therefore cannot be used to locate the GOE.

5.3. Origin of the small nonzero $\Delta^{33}S$ and $\Delta^{36}S$ signals in the Huronian

Multiple hypotheses may be able to explain the measured S isotope values in the Huronian pyrrhotites. Below, we explore these possibilities.

5.3.1. Homogenization of MIF signals by regional metamorphism. It is likely that the pyrrhotite in the studied drill cores formed by reaction of sedimentary pyrite during low-grade metamorphism. Theoretically, two general processes can lead to the transformation from pyrite (FeS_2) to pyrrhotite ($Fe_{0.8-1}S$): (1) gaining iron via reactions with Fe oxide or Fe-bearing silicates or (2) losing sulfur via metamorphic breakdown of pyrite into hydrogen sulfide or sulfur dioxide (Reuschel *et al.,* 2012; Asael *et al.,* 2013).

In the first scenario, although very few Fe oxide minerals are found surrounding the sulfide minerals (Fig. 4B, 4C) and are probably late alteration in origin, it is unlikely that iron

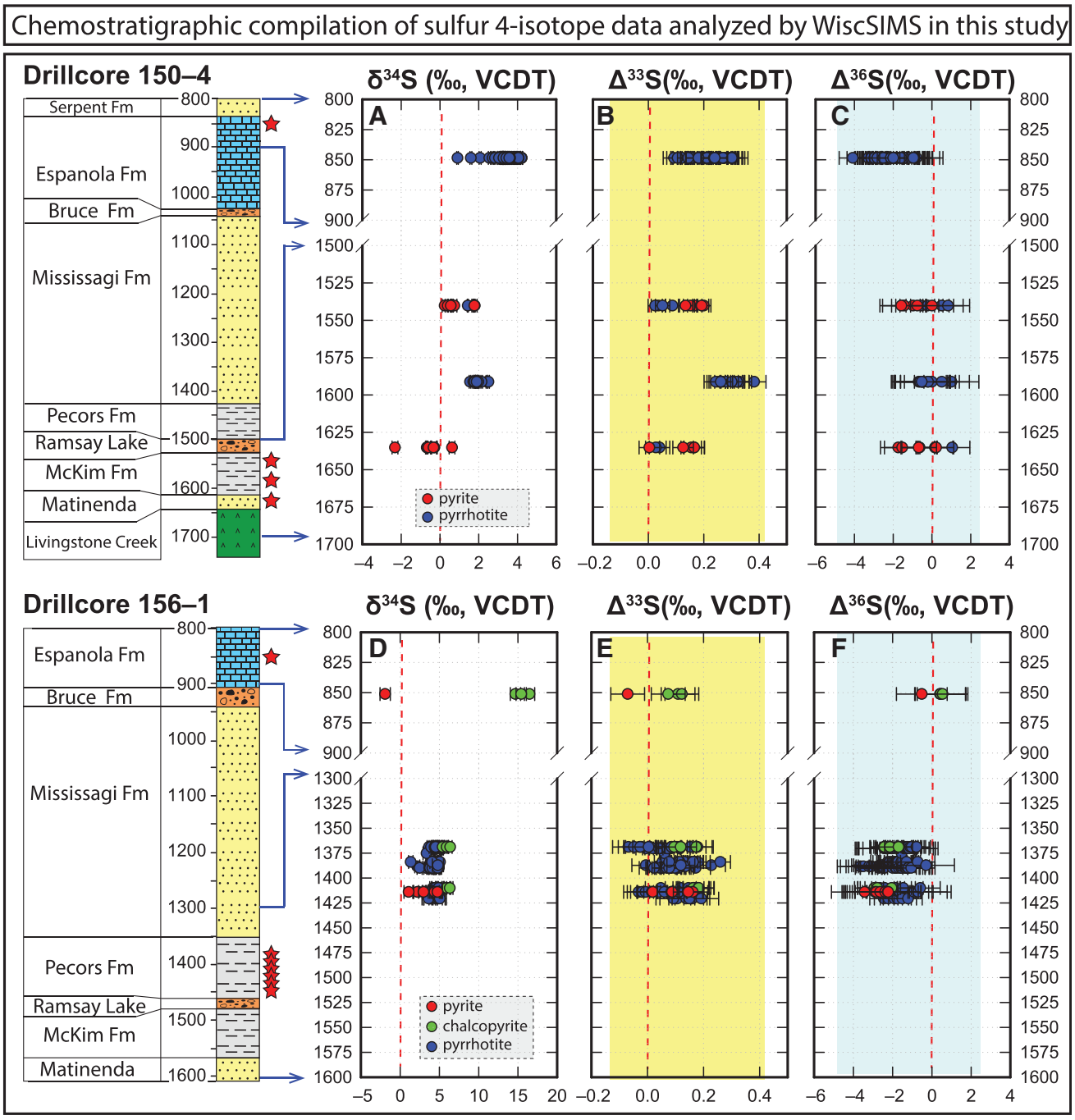

FIG. 9. Compiled multiple S isotope chemostratigraphy of the two studied drill cores in the Huronian Supergroup. All the sulfur four-isotope data were measured at WiscSIMS with improved methods (Ushikubo *et al.,* 2014) from this study. The highlighted color bands are the range for $\Delta^{33}S$ and $\Delta^{36}S$. Analytical uncertainty is the measured 2SD reproducibility on the UWPy-1 pyrite standard. Red stars alongside the lithology column mark the stratigraphic position of analyzed samples in this study.

oxide is a sufficient source of iron given the rarity of Fe oxide minerals in the studied interval (below the red beds in the Lorrain Formation). However, chlorite exists in close association with pyrrhotite (Fig. 3) and may have been a source of iron during pyrite–pyrrhotite transformation.

In the second scenario, metamorphic desulfidation reactions of pyrite can evolve either SO_2 (via reaction $FeS_2 + O_2 = FeS + SO_2$) or H_2S (via the reaction $FeS_2 + H_2 = FeS + H_2S$), depending on the redox conditions of metamorphism. If the former occurred, the $\delta^{34}S$ value of pyrrhotite would decrease compared with preexisting pyrite due to liberation of high-$\delta^{34}S$ SO_2. If the latter occurred, the $\delta^{34}S$ value of pyrrhotite would increase compared with preexisting pyrite due to liberation of low-$\delta^{34}S$ H_2S (Ohmoto, 1986). However, if no external source of MIF-bearing sulfur was involved in the formation of the Huronian sulfides, these

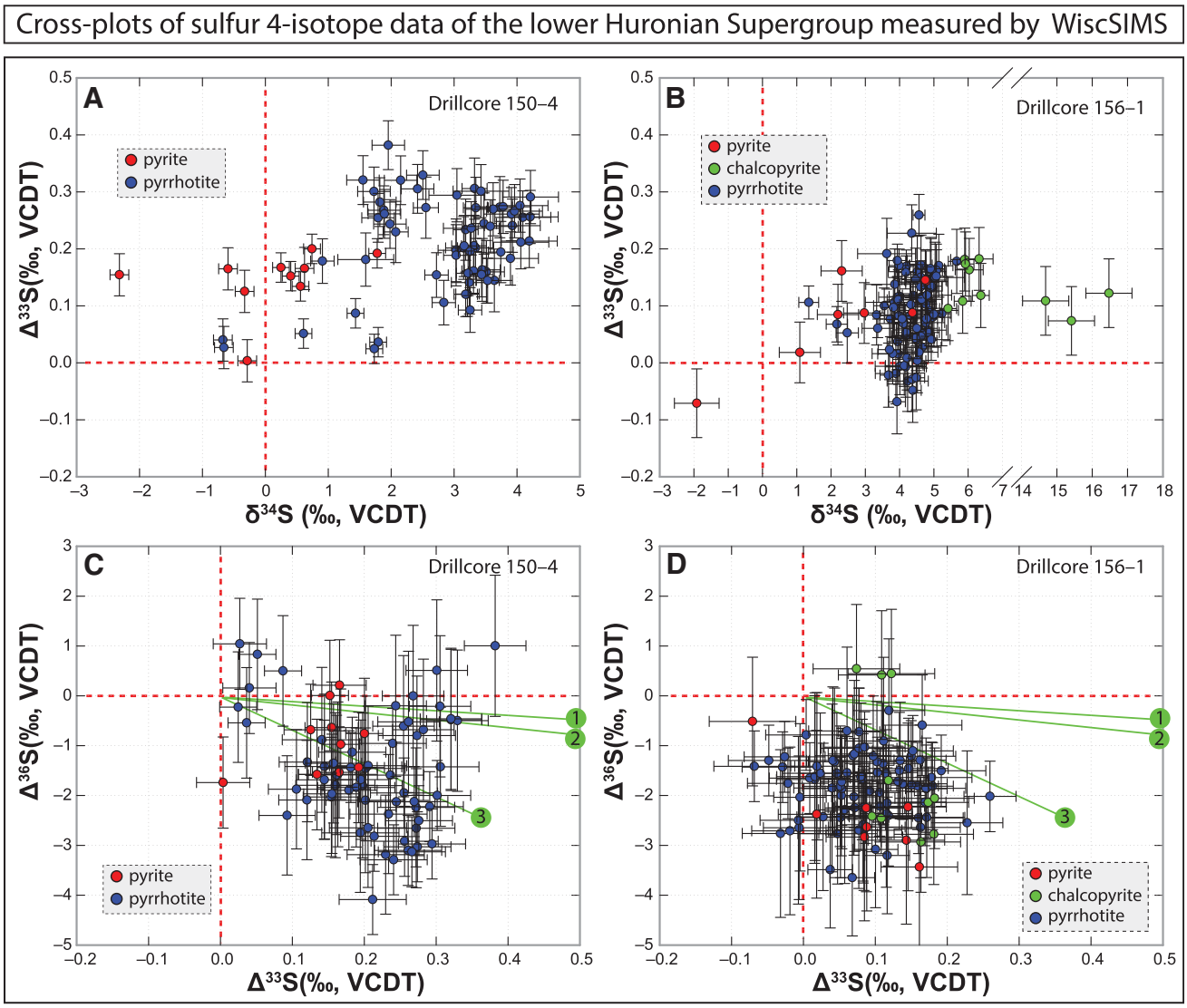

FIG. 10. Cross-plots of $\delta^{34}S$ versus $\Delta^{33}S$ and $\Delta^{33}S$ versus $\Delta^{36}S$ for SIMS analysis of sulfides in drill cores 150–4 and 156–1 of the Huronian Supergroup. The green lines 1, 2, 3 in panels C and D represent the Neoarchean–Paleoproterozoic slope ($\Delta^{36}S/\Delta^{33}S = ca.\ -0.9$), the Mesoarchean slope ($\Delta^{36}S/\Delta^{33}S = ca.\ -1.5$), and the theoretical MDF slope ($\Delta^{36}S/\Delta^{33}S = ca.\ -6.85$), respectively (Farquhar *et al.,* 2000; Ono *et al.,* 2006).

mass-dependent processes would neither create new MIF-S signatures nor destroy the original bulk MIF-S signatures. The dominant effect of regional metamorphism on $\Delta^{33}S$ or $\Delta^{36}S$ would be to homogenize and mute the variability of any preexisting MIF signals.

Although the Huronian sulfides may have experienced postdepositional desulfidation reactions and homogenization in chemical composition, we regard that the measured $\Delta^{33}S$ values may not deviate far from the average (whole rock) primary values. Given the rarity of very negative $\Delta^{33}S$ values in pyrite at that time, to achieve a homogenized $\Delta^{33}S$ near 0 value, it is unlikely that the $\Delta^{33}S$ values of the primary Huronian sulfides can be significantly positive before homogenization by regional metamorphism. Supporting evidence for this view also comes from published bulk rock data of the McKim and Pecors formations (Wing *et al.,* 2002, 2004). The bulk $\Delta^{33}S$ values of these two formations ranges from +0.22‰ to 0‰, which show similarly small and nonzero values compared with the SIMS data in this study.

5.3.2. Recycling of older MIF signals. It is also possible that fluids with preexisting MIF-S signals that are derived from *recycled* detrital pyrite may have overprinted the studied Huronian samples, resulting in the overall small MIF-S signals in the measured sections. A similar scenario has been used to explain the existence of small MIF-S signals during or shortly after the GOE when they were still not yet eliminated by chemical weathering and sediment dilution (Reinhard *et al.,* 2013).

In this study, although only samples that were deposited in marine facies were investigated in an effort to avoid detrital pyrite (see Section 3.1), the clearest evidence—rounded detrital grains—would be destroyed by metamorphic recrystallization. It is thus possible that MIF-S signals

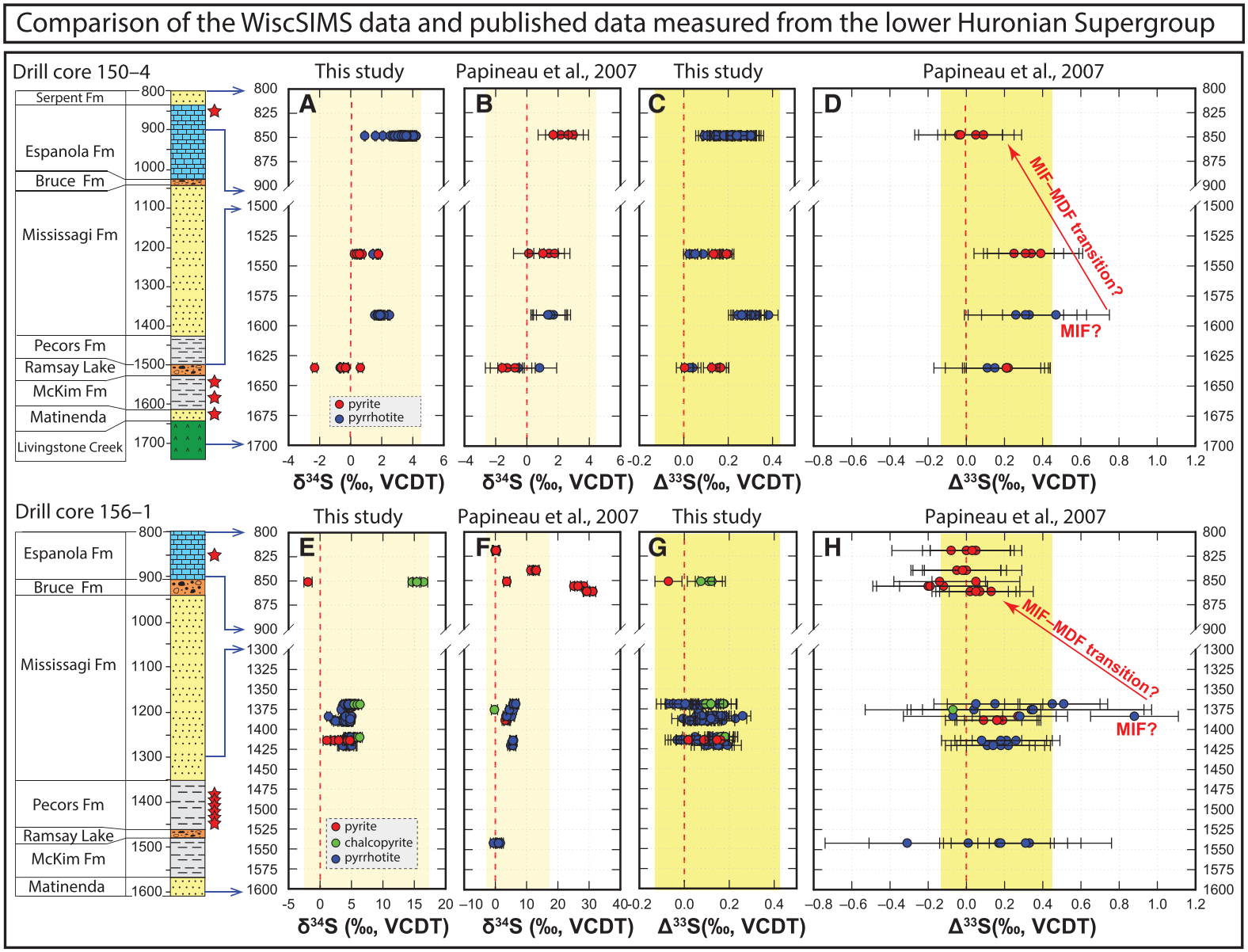

FIG. 11. A comparison between the data published in an early study (Papineau *et al.*, 2007) and the new data set analyzed by WiscSIMS in this study. Highlighted color bands mark the data ranges of the lower Huronian Supergroup from this study. See the main text for detailed discussion.

from older sediments may have been remobilized. It is also possible that MIF signals can be mobilized by fluids from these detrital grains or from older rocks. For example, an independent study of S three-isotopes of detrital pyrite and pyrite overgrowths in the fluvial-deltaic Mississagi Formation of the Huronian Supergroup shows $\Delta^{33}S$ values ranging from *ca.* −2‰ to ca. +1‰ (Ulrich *et al.,* 2011). These detrital pyrites can be a potential source of the measured MIF-S signals in this study. More studies are suggested to further evaluate the contribution of recycled MIF-S signals from late fluids in this region.

5.3.3. Dilution of MIF signals by magmatic fluids. Hypothetically, the overall small $\Delta^{33}S$ or $\Delta^{36}S$ signals can also result from the dilution of MIF signals by a magmatic reservoir with MDF signals. This process has been used to explain the general near-zero $\Delta^{33}S$ values in the Archean gold deposits in Western Australia (Xue *et al.,* 2013). Notably, the Huronian Supergroup was intruded by multiple dikes (Fig. 1), including the Nipissing diabase at *ca.* 2.22 Ga (Fig. 2) (Corfu and Andrews, 1986; Mossman *et al.,* 1993), which may have indeed caused a significant dilution of the primary MIF-S signals. If true, potentially primary large MIF-S signals of the Huronian Supergroup may have been significantly erased by a large volume of MDF-bearing magmatic fluids.

Based on a mass balance perspective, if the primary MIF signal in the Huronian is pronounced, the MDF-bearing magmatic fluids should be very large in volume in order to achieve near-zero values. However, in light of the overall small $\Delta^{33}S$ or $\Delta^{36}S$ values analyzed from the remaining pyrite grains, the magmatic fluids that are needed to achieve overall near-zero values can be relatively small in volume. More studies are suggested to further evaluate the overall influence of late magmatic fluids in this region.

5.3.4. Small $\Delta^{33}S$ or $\Delta^{36}S$ signals produced by MDF. The small $\Delta^{33}S$ or $\Delta^{36}S$ signals in the Huronian can also be explained by the occurrence of MDF. Lab experiments of post-Archean samples show small magnitude of $\Delta^{33}S$ (from 0‰ to *ca.* 0.4‰) or $\Delta^{36}S$ (from −2.5‰ to 0‰) signals in sedimentary sulfides, which have been explained by the occurrence of MDF (Ono *et al.,* 2006).

It was revealed that these small MDF-produced $\Delta^{33}S$ and $\Delta^{36}S$ signals have a distinctive $\Delta^{36}S/\Delta^{33}S$ slope of −6.85, which can be used as a tool to distinguish the origin of small $\Delta^{36}S$ and $\Delta^{33}S$ signals (Ono *et al.,* 2006). However, due to the small range of values and larger uncertainty of data generated by SIMS compared with the conventional gas source mass spectrometer, it is not feasible to extract a reliable $\Delta^{36}S/\Delta^{33}S$ slope based on the current SIMS data set (Fig. 10). Therefore, conventional analysis of larger samples by gas source mass spectrometry may yield better precision and reveal subtle correlation even though the range of values is so small.

In summary, we propose a metamorphic origin for the Huronian pyrrhotite based on detailed investigation of petrography and mineral assemblages. Metamorphism tends to homogenize and mute variability but not create or destroy the MIF-S signals. Recycled older MIF signals, dilution by magmatic fluids, or the occurrence of MDF may have also contributed to the generation of the overall small MIF signals in the studied samples. Therefore, in contrast to the previous study on the same successions (Papineau *et al.,* 2007), we argue that the precise location of the MIF–MDF transition in the Huronian remains unsolved. This putative MIF–MDF transition may have already been erased by postdepositional processes in the lower Huronian supergroup or may be located in the upper Huronian Supergroup.

5.4. Implications on the GOE

5.4.1. An evolving concept of the GOE. Although the existence of the GOE is indicated by sedimentological observations, the placement of the GOE in the Huronian stratigraphy is still ambiguous. Before discussing the GOE in the Huronian, it should be noted that the criteria to identify the GOE may vary among different authors.

Largely based on sedimentological observations, the GOE has been interpreted as a long time interval between ~2.4 and ~2.0 Ga, which is characterized by a gradual transition from reducing atmosphere to weakly oxygenated redox conditions in atmosphere and shallow oceans (Holland, 2002, 2006; Bekker, 2014; Gumsley *et al.,* 2017). The discovery of the intimate response of time-series S four-isotopes (*i.e.,* MIF–MDF transition) to the rise of atmospheric oxygen makes it possible to pinpoint the timing of this putative event to be *ca.* 2.45 Ga (Farquhar *et al.,* 2000; Farquhar and Wing, 2003, 2005). Thus, the GOE has been identified in two ways. In a broader sense, the GOE refers to a long-term sedimentological transition in the Paleoproterozoic with possible oscillations in atmospheric oxygen levels (Holland, 2006; Gumsley *et al.,* 2017). In a narrower sense, the GOE is defined by the S isotope transition from MIF to MDF. The latter has been increasingly adopted in studies of individual sections of the Paleoproterozoic (Guo *et al.,* 2009; Williford *et al.,* 2011; Luo *et al.,* 2016).

The threshold $\Delta^{33}S$ value that marks the MIF–MDF transition and the GOE is uncertain. For example, chemostratigraphic studies from South Africa reveal a profound sulfur isotope transition from large MIF signals ($\Delta^{33}S$ up to *ca.* +7‰, $\Delta^{36}S$ down to *ca.* −7‰) and overall positive $\delta^{34}S$, to the onset of MDF with large MDF negative excursions in $\delta^{34}S$ (down to *ca.* −30‰) based on bulk S isotope analysis (Fig. 12) (Cameron, 1982; Bekker *et al.,* 2004; Luo *et al.,* 2016). By defining the GOE as a transition to $|\Delta^{33}S|$ values <0.5‰ followed by a sharp negative $\delta^{34}S$ shift, the GOE was thereby pinpointed at *ca.* 3 m below the stratigraphic boundary between the Duitschland/Rooihoogte Formation and the Timeball Hill Formation in South Africa (Fig. 12) (Luo *et al.,* 2016). Similarly, a detailed study of the Meteorite Bore Member of the Kungarra Formation (Turee Creek Group) from Western Australia reveals MIF signals with nonzero $\Delta^{33}S$ values ranging from −0.83‰ to 0.96‰ (± 0.09‰, 2SD), which have been interpreted to represent the final stage of the GOE (Williford *et al.,* 2011). In this case, the threshold value of $|\Delta^{33}S| = ca.$ 0.9‰ has been used to define the MIF–MDF transition and the GOE. Regardless of different threshold $|\Delta^{33}S|$ values in different studies, the approach of defining the GOE by MIF–MDF transition is practical in detailed chemostratigraphic studies of individual geological sections.

5.4.2. Differences of the S isotope patterns of the GOE sections. The published and new S isotope data show different features among the GOE sections in South Africa (Guo

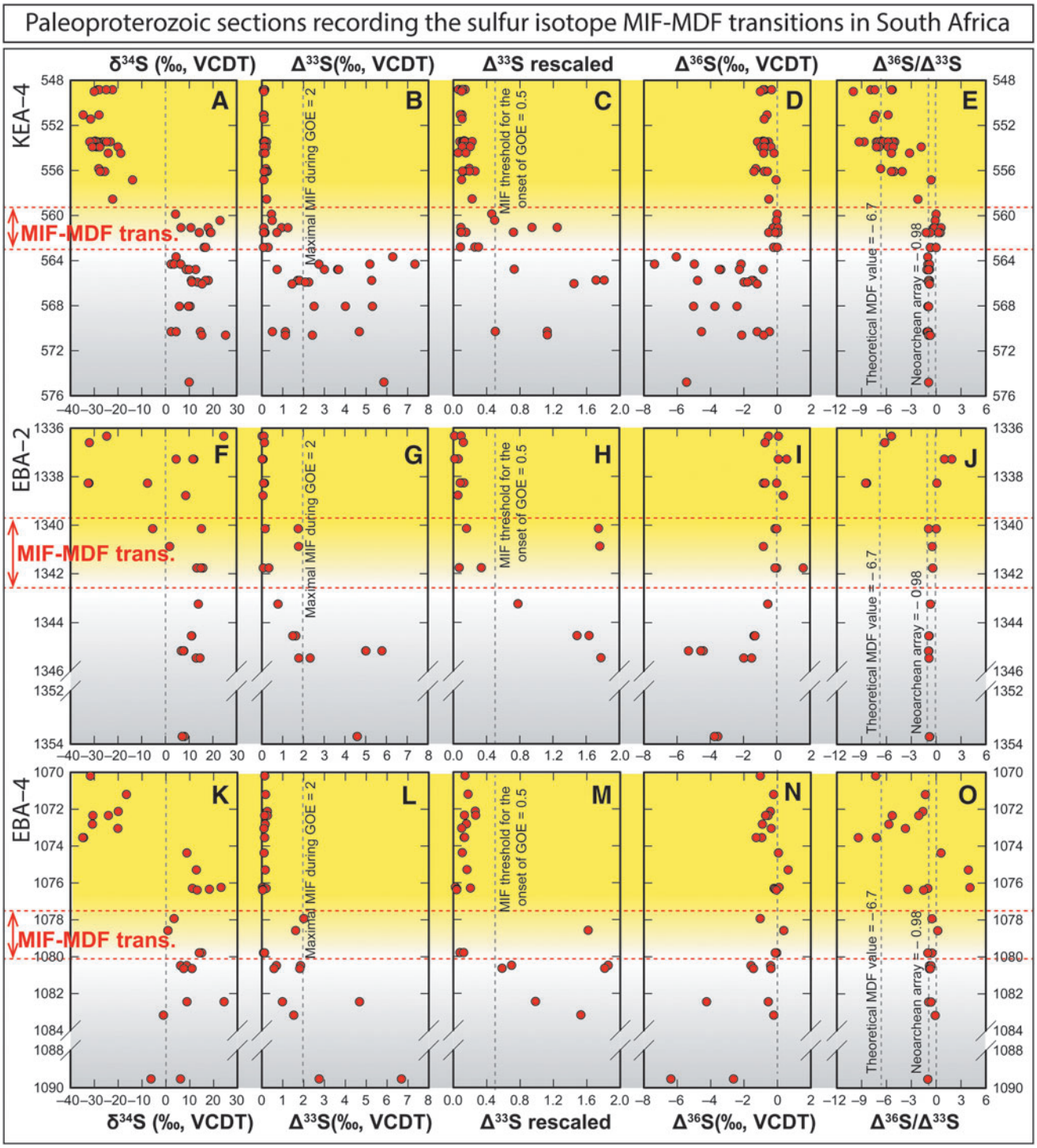

FIG. 12. Multiple-S isotope profiles of Paleoproterozoic strata spanning the GOE in South Africa. Data in the *y* axis represent stratigraphic depth (in meters) of the drill cores. Source from the work of Luo *et al.* (2016). By defining the GOE as a transition to $|\Delta^{33}S|$ values <0.5‰, the GOE was pinpointed at *ca.* 3 m below the stratigraphic boundary between the Duitschland/Rooihoogte Formation and the Timeball Hill Formation in South Africa. For detailed information on stratigraphy, please refer to the work of Luo *et al.* (2016).

et al., 2009; Luo *et al.,* 2016; Gumsley *et al.,* 2017), Western Australia (Williford *et al.,* 2011), and North America (this study). We propose that the differences among these sections may result from the difference in analytical methods (bulk vs. SIMS) and the postdepositional history (early authigenic vs. late-stage metamorphism) of different basins. If the samples are well preserved, the integrated scanning electron microscopy (SEM) and secondary ion mass spectrometry (SIMS) techniques have the capability to distinguish and target small domains in different types of sulfide and to distinguish sulfur isotope signals that would otherwise be lost by bulk analysis. Therefore, a data set measured by SIMS provides more

complexities compared with data analyzed from bulk samples (*e.g.,* Williford *et al.,* 2011).

In addition to analytical methods, various postdepositional history may also have contributed to the different patterns in S isotope profiles. In the studied Huronian Supergroup, low-grade metamorphism or late fluid activities may have influenced the S isotope values. Therefore, caution is needed when conducting direct stratigraphic correlations among these sections (Hoffman, 2013; Gumsley *et al.,* 2017).

The accuracy of geochronological data of the Paleoproterozoic successions is also critical to our understanding of the detailed dynamics of the GOE (Rasmussen *et al.,* 2013; Gumsley *et al.,* 2017). A recent compilation suggests that MIF-S could potentially be lost from the record and reappear (Gumsley *et al.,* 2017), either due to a fluctuating atmospheric composition (Gumsley *et al.,* 2017) or due to geological reworking of older anomalous MIF-S sources (Reinhard *et al.,* 2013). Therefore, the reconstruction of the GOE by chemostratigraphy of multiple S-isotopes should be based on an accurate geochronological framework.

6. Conclusions

(1) In this study, two drill cores of the Huronian Supergroup were revisited and analyzed for S four-isotopes in pyrite, chalcopyrite, and pyrrhotite. Based on the mineral assemblages and S isotopic compositions, it is proposed that the dominance of pyrrhotite in the studied drill cores results from regional metamorphism, instead of early authigenesis.

(2) The new $\Delta^{33}S$ and $\Delta^{36}S$ data in this study show homogeneous values at micrometer and millimeter scales. They all fall within a narrow range. The new $\Delta^{33}S$ data have improved precision compared to earlier studies. Small but analytically resolvable nonzero signals of $\Delta^{33}S$ (from $-0.07‰$ to $+0.38‰$) and $\Delta^{36}S$ (from $-4.1‰$ to $+1.0‰$) persist throughout the entire lower Huronian Supergroup. Neither pronounced MIF-S signals nor a MIF–MDF transition are seen in this study (Figs. 9 and 11).

(3) Four scenarios were discussed on the origin of small nonzero $\Delta^{33}S$ and $\Delta^{36}S$ signals: muted variability by regional metamorphism, recycling of older pyrite, dilution by magmatic fluids, and the genesis by MDF. Metamorphic recrystallization homogenized any isotope zoning in original sediments, and would have muted S isotope variability, but did not create or destroy the MIF-S signals. The involvement of recycled older MIF signals, magmatic fluids with MDF signals, or small nonzero signals produced by MDF may have also contributed to the overall muted signals. Therefore, we argue that the precise location of the MIF–MDF transition remains unsolved and may have been erased by postdepositional processes in the lower Huronian Supergroup, or may be located in the upper Huronian Supergroup. The previously proposed MIF–MDF transition in the Huronian (Papineau *et al.,* 2007) is not supported in this study and cannot be used to infer the GOE in North America.

(4) This study demonstrates that the SEM–SIMS technique provides fresh insight for unraveling the complexities of the GOE-bearing strata. The differences among Paleoproterozoic sections may result from differences in analytical methods (bulk vs. SIMS) and the postdepositional history (early authigenic vs. late-stage metamorphism) of different basins.

Acknowledgments

This study is supported by the NASA Astrobiology Institute (NNA13AA94A). The WiscSIMS Lab is supported by NSF (EAR–1355590, –1658823) and UW–Madison. The authors acknowledge Phillip Gopon, Tina Hill, and Bil Schneider for the assistance in the SEM lab; Brian Hess, James Kern, and Maciej Śliwiński for assistance in sample preparation; and Noriko Kita for the assistance in the WiscSIMS lab at UW–Madison. We also thank James Farquhar and Genming Luo for helpful comments, Dominic Papineau for sharing the spreadsheet of the published data, and John Walmsley, Dan Farrow, and Anthony Pace from the Ontario Geological Survey at Sault Ste. Marie for the access of the studied drill cores. This manuscript has been improved by constructive comments from two anonymous reviewers.

Author Disclosure Statement

No competing financial interests exist.

References

Asael, D., Tissot, F.L.H., Reinhard, C.T., Rouxel, O., Dauphas, N., Lyons, T.W., Ponzevera, E., Liorzou, C., and Chéron, S. (2013) Coupled molybdenum, iron and uranium stable isotopes as oceanic paleoredox proxies during the Paleoproterozoic Shunga Event. *Chem Geol* 362:193–210.

Bekker, A. (2014) Great Oxygenation Event. In *Encyclopedia of Astrobiology,* edited by R. Amils, M. Gargaud, J. Cernicharo Quintanilla, H.J. Cleaves, W.M. Irvine, D. Pinti, and M. Visos, Springer, Berlin, pp 1–9.

Bekker, A. and Kaufman, A.J. (2007) Oxidative forcing of global climate change: a biogeochemical record across the oldest Paleoproterozoic ice age in North America. *Earth Planet Sci Lett* 258:486–499.

Bekker, A., Holland, H.D., Wang, P.-L., Rumble, D., III, Stein, H.J., Hannah, J.L., Coetzee, L.L., and Beukes, N.J. (2004) Dating the rise of atmospheric oxygen. *Nature* 427:117–120.

Cabral, R.A., Jackson, M.G., Rose-Koga, E.F., Koga, K.T., Whitehouse, M.J., Antonelli, M.A., Farquhar, J., Day, J.M., and Hauri, E.H. (2013) Anomalous sulphur isotopes in plume lavas reveal deep mantle storage of Archaean crust. *Nature* 496:490–493.

Cameron, E.M. (1982) Sulphate and sulphate reduction in early Precambrian oceans. *Nature* 296:145–148.

Card, K. (1978) Metamorphism of the middle Precambrian (Aphebian) rocks of the eastern Southern Province. In *Metamorphism in the Canadian Shield,* edited by J.A. Fraser and W.W. Heywoods, Geological Survey of Canada Paper 78–10, Geological Survey of Canada, Ottawa, pp 269–282.

Chandler, F.W. (1988) Diagenesis of sabkha-related, sulphate nodules in the early Proterozoic Gordon Lake formation, Ontario, Canada. *Carbonates and Evaporites* 3:75–94.

Cloud, P. (1972) A working model of the primitive Earth. *Am J Sci* 272:537–548.

Cloud, P. (1976) Beginnings of biospheric evolution and their biogeochemical consequences. *Paleobiology* 2:351–387.

Cloud, P.E. (1968) Atmospheric and hydrospheric evolution on the primitive Earth. *Science* 160:729–736.

Corfu, F. and Andrews, A. (1986) A U–Pb age for mineralized Nipissing diabase, Gowganda, Ontario. *Can J Earth Sci* 23: 107–109.

Crowe, D.E. and Vaughan, R.G. (1996) Characterization and use of isotopically homogeneous standards for *in situ* laser microprobe analysis of $^{34}S/^{32}S$ ratios. *Am Mineral* 81:187–193.

Ding, T., Valkiers, S., Kipphardt, H., De Bièvre, P., Taylor, P.D.P., Gonfiantini, R., and Krouse, R. (2001) Calibrated sulfur isotope abundance ratios of three IAEA sulfur isotope reference materials and V-CDT with a reassessment of the atomic weight of sulfur. *Geochim Cosmochim Acta* 65: 2433–2437.

Donovan, J., Kremser, D., Fournelle, J., and Goemann, K. (2018) *Probe for Windows User's Guide and Reference, Enterprise Edition,* Probe Software, Inc., Eugene, OR.

Dutkiewicz, A., Volk, H., George, S.C., Ridley, J., and Buick, R. (2006) Biomarkers from Huronian oil-bearing fluid inclusions: an uncontaminated record of life before the Great Oxidation Event. *Geology* 34:437–440.

Farquhar, J. and Wing, B.A. (2003) Multiple sulfur isotopes and the evolution of the atmosphere. *Earth Planet Sci Lett* 213:1–13.

Farquhar, J. and Wing, B.A. (2005) The terrestrial record of stable sulphur isotopes: a review of the implications for evolution of Earth's sulphur cycle. In *Mineral Deposits and Earth Evolution,* Geological Society special publication no. 248, edited by I. Mcdonald, A.J. Boyce, I.B. Butler, R.J. Herrington, and D.A. Polyas, Geological Society, London, pp 167–177.

Farquhar, J., Bao, H., and Thiemens, M. (2000) Atmospheric influence of Earth's earliest sulfur cycle. *Science* 289:756–758.

Farquhar, J., Zerkle, A.L., and Bekker, A. (2011) Geological constraints on the origin of oxygenic photosynthesis. *Photosynth Res* 107:11–36.

Farquhar, J., Zerkle, A.L., and Bekker, A. (2014) Geologic and geochemical constraints on Earth's early atmosphere. In *Treatise on Geochemistry,* 2nd ed., edited by H.D. Holland and K.K. Turekians, Elsevier, Oxford, pp 91–138.

Ferrini, V., Fayek, M., De Vito, C., Mignardi, S., and Pignatti, J. (2010) Extreme sulphur isotope fractionation in the deep Cretaceous biosphere. *J Geol Soc London* 167:1009–1018.

Fischer, W.W., Fike, D.A., Johnson, J.E., Raub, T.D., Guan, Y., Kirschvink, J.L., and Eiler, J.M. (2014) SQUID–SIMS is a useful approach to uncover primary signals in the Archean sulfur cycle. *Proc Natl Acad Sci USA* 111:5468–5473.

Fischer, W.W., Hemp, J., and Johnson, J.E. (2016) Evolution of oxygenic photosynthesis. *Annu Rev Earth Planet Sci* 44: 647–683.

Goto, K.T., Sekine, Y., Suzuki, K., Tajika, E., Senda, R., Nozaki, T., Tada, R., Goto, K., Yamamoto, S., and Maruoka, T. (2013) Redox conditions in the atmosphere and shallow-marine environments during the first Huronian deglaciation: insights from Os isotopes and redox-sensitive elements. *Earth Planet Sci Lett* 376:145–154.

Gumsley, A.P., Chamberlain, K.R., Bleeker, W., Söderlund, U., de Kock, M.O., Larsson, E.R., and Bekker, A. (2017) Timing and tempo of the Great Oxidation Event. *Proc Natl Acad Sci USA* 114:1811–1816.

Guo, Q., Strauss, H., Kaufman, A.J., Schröder, S., Gutzmer, J., Wing, B., Baker, M.A., Bekker, A., Jin, Q., Kim, S.-T., and Farquhar, J. (2009) Reconstructing Earth's surface oxidation across the Archean–Proterozoic transition. *Geology* 37: 399–402.

Hannah, J.L., Bekker, A., Stein, H.J., Markey, R.J., and Holland, H.D. (2004) Primitive Os and 2316 Ma age for marine shale: implications for Paleoproterozoic glacial events and the rise of atmospheric oxygen. *Earth Planet Sci Lett* 225:43–52.

Hattori, K., Krouse, H.R., and Campbell, F.A. (1983) The start of sulfur oxidation in continental environments: about 2.2×10^9 years ago. *Science* 221:549–551.

Hazen, R.M. and Ferry, J.M. (2010) Mineral evolution: mineralogy in the fourth dimension. *Elements* 6:9–12.

Hazen, R.M., Papineau, D., Bleeker, W., Downs, R.T., Ferry, J.M., McCoy, T.J., Sverjensky, D.A., and Yang, H. (2008) Mineral evolution. *Am Mineral* 93:1693–1720.

Hill, C., Corcoran, P.L., Aranha, R., and Longstaffe, F.J. (2016) Microbially induced sedimentary structures in the Paleoproterozoic, upper Huronian Supergroup, Canada. *Precambrian Res* 281:155–165.

Hoffman, P.F. (2013) The Great Oxidation and a Siderian snowball Earth: MIF-S based correlation of Paleoproterozoic glacial epochs. *Chem Geol* 362:143–156.

Holland, H.D. (1978) *The Chemistry of the Atmosphere and Oceans,* Wiley-Interscience, New York.

Holland, H.D. (1984) *The Chemical Evolution of the Atmosphere and Oceans,* Princeton University Press, Princeton, NJ.

Holland, H.D. (2002) Volcanic gases, black smokers, and the Great Oxidation Event. *Geochim Cosmochim Acta* 66: 3811–3826.

Holland, H.D. (2006) The oxygenation of the atmosphere and oceans. *Philos Trans R Soc Lond B Biol Sci* 361:903–915.

Holland, H.D., Lazar, B., and McCaffrey, M. (1986) Evolution of the atmosphere and oceans. *Nature* 320:27–33.

Honsho, C., Yamazaki, T., Ura, T., Okino, K., Morozumi, H., and Ueda, S. (2016) Magnetic anomalies associated with abundant production of pyrrhotite in a sulfide deposit in the Okinawa Trough, Japan. *Geochem Geophys Geosyst* 17:4413–4424.

Horng, C.-S. and Roberts, A.P. (2006) Authigenic or detrital origin of pyrrhotite in sediments? Resolving a paleomagnetic conundrum. *Earth Planet Sci Lett* 241:750–762.

Johnson, J.E., Gerpheide, A., Lamb, M.P., and Fischer, W.W. (2014) O_2 constraints from Paleoproterozoic detrital pyrite and uraninite. *Geol Soc Am Bull* 126:813–830.

Johnston, D.T. (2011) Multiple sulfur isotopes and the evolution of Earth's surface sulfur cycle. *Earth-Science Reviews* 106: 161–183.

Jones, D., Hartley, J., Frisch, G., Purnell, M., and Darras, L. (2012) Non-destructive, safe removal of conductive metal coatings from fossils: a new solution. *Palaeontologia Electronica* 15, 15.2.4T.

Kars, M. and Kodama, K. (2015) Authigenesis of magnetic minerals in gas hydrate-bearing sediments in the Nankai Trough, offshore Japan. *Geochem Geophys Geosyst* 16: 947–961.

Kasting, J.F., Holland, H.D., and Kump, L.R. (1992) Atmospheric evolution: the rise of oxygen. In *The Proterozoic Biosphere: A Multidisciplinary Study,* edited by J.W. Schopf and C. Kleins, Cambridge University Press, New York, pp 159–164.

Ketchum, K.Y., Heaman, L.M., Bennett, G., and Hughes, D.J. (2013) Age, petrogenesis and tectonic setting of the Thessalon volcanic rocks, Huronian Supergroup, Canada. *Precambrian Res* 233:144–172.

Kita, N.T., Huberty, J.M., Kozdon, R., Beard, B.L., and Valley, J.W. (2011) High-precision SIMS oxygen, sulfur and iron stable isotope analyses of geological materials: accuracy, surface topography and crystal orientation. *Surf Interface Anal* 43:427–431.

Knoll, A.H. (2015) Paleobiological perspectives on early microbial evolution. *Cold Spring Harb Perspect Biol* 7, doi: 10.1101/cshperspect.a018093.

Knoll, A.H., Bergmann, K.D., and Strauss, J.V. (2016) Life: the first two billion years. *Philos Trans R Soc Lond B Biol Sci* 371, doi:10.1098/rstb.2015.0493.

Kohn, M.J., Riciputi, L.R., Stakes, D., and Orange, D.L. (1998) Sulfur isotope variability in biogenic pyrite: reflections of heterogeneous bacterial colonization? *Am Mineral* 83:1454–1468.

Kozdon, R., Kita, N.T., Huberty, J.M., Fournelle, J.H., Johnson, C.A., and Valley, J.W. (2010) *In situ* sulfur isotope analysis of sulfide minerals by SIMS: precision and accuracy, with application to thermometry of ~3.5 Ga Pilbara cherts. *Chem Geol* 275:243–253.

Krogh, T.E., Davis, D.W., and Corfu, F. (1984) Precise U–Pb zircon and baddeleyite ages for the Sudbury area. In *The Geology and Ore Deposits of the Sudbury Structure,* edited by E.G. Pye, A.J. Naldrett, and P.E. Giblins, Ontario Ministry of Natural Resources, Toronto, pp 431–446.

Kump, L.R. (2008) The rise of atmospheric oxygen. *Nature* 451:277–278.

Larrasoaña, J.C., Roberts, A.P., Musgrave, R.J., Gràcia, E., Piñero, E., Vega, M., and Martínez-Ruiz, F. (2007) Diagenetic formation of greigite and pyrrhotite in gas hydrate marine sedimentary systems. *Earth Planet Sci Lett* 261:350–366.

Lin, Z., Sun, X., Peckmann, J., Lu, Y., Xu, L., Strauss, H., Zhou, H., Gong, J., Lu, H., and Teichert, B.M.A. (2016) How sulfate-driven anaerobic oxidation of methane affects the sulfur isotopic composition of pyrite: a SIMS study from the South China Sea. *Chem Geol* 440:26–41.

Liu, X.-M., Kah, L.C., Knoll, A.H., Cui, H., Kaufman, A.J., Shahar, A., and Hazen, R.M. (2016) Tracing Earth's O_2 evolution using Zn/Fe ratios in marine carbonates. *Geochem Persp Lett* 2:24–34.

Luo, G., Ono, S., Beukes, N.J., Wang, D.T., Xie, S., and Summons, R.E. (2016) Rapid oxygenation of Earth's atmosphere 2.33 billion years ago. *Sci Adv* 2, doi:10.1126/sciadv.1600134.

Lyons, T.W., Reinhard, C.T., and Planavsky, N.J. (2014) The rise of oxygen in Earth's early ocean and atmosphere. *Nature* 506:307–315.

Magnall, J.M., Gleeson, S.A., Stern, R.A., Newton, R.J., Poulton, S.W., and Paradis, S. (2016) Open system sulphate reduction in a diagenetic environment—isotopic analysis of barite ($\delta^{34}S$ and $\delta^{18}O$) and pyrite ($\delta^{34}S$) from the Tom and Jason Late Devonian Zn–Pb–Ba deposits, Selwyn Basin, Canada. *Geochim Cosmochim Acta* 180:146–163.

McLoughlin, N., Grosch, E.G., Kilburn, M.R., and Wacey, D. (2012) Sulfur isotope evidence for a Paleoarchean subseafloor biosphere, Barberton, South Africa. *Geology* 40:1031–1034.

Melezhik, V.A., Young, G.M., Eriksson, P.G., Altermann, W., Kump, L.R., and Lepland, A. (2013) Huronian-age glaciation. In *Reading the Archive of Earth's Oxygenation: Volume 3: Global Events and the Fennoscandian Arctic Russia–Drilling Early Earth Project,* edited by V.A. Melezhik, A.R. Prave, E.J. Hanski, A.E. Fallick, A. Lepland, L.R. Kump, and H. Strausss, Springer, Berlin, pp 1059–1109.

Minguez, D., Kodama, K.P., and Engelder, T. (2016) Paleomagnetism of the Oatka Creek member of the Marcellus Formation: a Devonian paleopole for North America. *Geol Soc Am Bull* 128:707–718.

Mossman, D.J., Nagy, B., and Davis, D.W. (1993) Hydrothermal alteration of organic matter in uranium ores, Elliot Lake, Canada: implications for selected organic-rich deposits. *Geochim Cosmochim Acta* 57:3251–3259.

Nesbitt, H.W. and Young, G.M. (1982) Early Proterozoic climates and plate motions inferred from major element chemistry of lutites. *Nature* 299:715–717.

Ohmoto, H. (1986) Stable isotope geochemistry of ore deposits. In *Stable Isotopes in High Temperature Geological Processes,* Reviews in Mineralogy Volume 16, edited by J.W. Valley, H.P. Taylor, and J.R. O'Neil, Mineralogical Society of America, Washington, DC, pp 491–559.

Ohmoto, H. and Rye, R.O. (1979) Isotopes of sulfur and carbon. In *Geochemistry of Hydrothermal Ore Deposits,* edited by H.L. Barness, John Wiley & Sons, New York, pp 509–567.

Olson S.L., Schwieterman E.W., Reinhard C.T., and Lyons T.W. (2018) Earth: Atmospheric Evolution of a Habitable Planet. In *Handbook of Exoplanets,* edited by H.J. Deeg and J.A. Belmontes, Springer International Publishing, Cham, p 1–37. http://doi.org/10.1007/978-3-319-30648-3_189-1.

Ono S. (2017) Photochemistry of sulfur dioxide and the origin of mass-independent isotope fractionation in Earth's atmosphere. *Annu Rev Earth Planet Sci* 45:301–329.

Ono, S., Wing, B., Johnston, D., Farquhar, J., and Rumble, D. (2006) Mass-dependent fractionation of quadruple stable sulfur isotope system as a new tracer of sulfur biogeochemical cycles. *Geochim Cosmochim Acta* 70:2238–2252.

Papineau, D., Mojzsis, S.J., Coath, C.D., Karhu, J.A., and McKeegan, K.D. (2005) Multiple sulfur isotopes of sulfides from sediments in the aftermath of Paleoproterozoic glaciations. *Geochim Cosmochim Acta* 69:5033–5060.

Papineau, D., Mojzsis, S.J., and Schmitt, A.K. (2007) Multiple sulfur isotopes from Paleoproterozoic Huronian interglacial sediments and the rise of atmospheric oxygen. *Earth Planet Sci Lett* 255:188–212.

Rasmussen, B. and Buick, R. (1999) Redox state of the Archean atmosphere: evidence from detrital heavy minerals in *ca.* 3250–2750 Ma sandstones from the Pilbara Craton, Australia. *Geology* 27:115–118.

Rasmussen, B., Bekker, A., and Fletcher, I.R. (2013) Correlation of Paleoproterozoic glaciations based on U–Pb zircon ages for tuff beds in the Transvaal and Huronian Supergroups. *Earth Planet Sci Lett* 382:173–180.

Reinhard, C.T., Planavsky, N.J., and Lyons, T.W. (2013) Long-term sedimentary recycling of rare sulphur isotope anomalies. *Nature* 497:100–103.

Reuschel, M., Melezhik, V.A., and Strauss, H. (2012) Sulfur isotopic trends and iron speciation from the c. 2.0 Ga Pilgujärvi Sedimentary Formation, NW Russia. *Precambrian Res* 196–197:193–203.

Reynolds, R.L., Fishman, N.S., Wanty, R.B., and Goldhaber, M.B. (1990) Iron sulfide minerals at Cement oil field, Oklahoma: implications for magnetic detection of oil fields. *Geol Soc Am Bull* 102:368–380.

Roscoe, S.M. (1969) *Huronian Rocks and Uraniferous Conglomerates in the Canadian Shield,* Geological Survey of Canada Paper 68–40, Department of Energy, Mines and Resources, Ottawa.

Roscoe, S.M. (1973) The Huronian Supergroup, a Paleoaphebian succession showing evidence of atmospheric evolution. In *Huronian Stratigraphy and Sedimentation,* Geological Association of Canada Special Paper 12, edited by G.M. Young, Marrais, Montreal, pp 31–47.

Seal, R.R. (2006) Sulfur isotope geochemistry of sulfide minerals. *Reviews in Mineralogy and Geochemistry* 61:633–677.

Sekine, Y., Suzuki, K., Senda, R., Goto, K.T., Tajika, E., Tada, R., Goto, K., Yamamoto, S., Ohkouchi, N., and Ogawa, N.O. (2011a) Osmium evidence for synchronicity between a rise in atmospheric oxygen and Palaeoproterozoic deglaciation. *Nat Commun* 2, doi:10.1038/ncomms1507.

Sekine, Y., Tajika, E., Tada, R., Hirai, T., Goto, K.T., Kuwatani, T., Goto, K., Yamamoto, S., Tachibana, S., and Isozaki, Y. (2011b) Manganese enrichment in the Gowganda Formation of the Huronian Supergroup: a highly oxidizing

shallow-marine environment after the last Huronian glaciation. *Earth Planet Sci Lett* 307:201–210.

Simpson, S.L., Boyce, A.J., Lambert, P., Lindgren, P., and Lee, M.R. (2017) Evidence for an impact-induced biosphere from the $\delta^{34}S$ signature of sulphides in the Rochechouart impact structure, France. *Earth Planet Sci Lett* 460:192–200.

Thomazo, C., Ader, M., Farquhar, J., and Philippot, P. (2009) Methanotrophs regulated atmospheric sulfur isotope anomalies during the Mesoarchean (Tumbiana Formation, Western Australia). *Earth Planet Sci Lett* 279:65–75.

Ulrich, T., Long, D.G.F., Kamber, B.S., and Whitehouse, M.J. (2011) *In situ* trace element and sulfur isotope analysis of pyrite in a Paleoproterozoic gold placer deposit, Pardo and Clement Townships, Ontario, Canada. *Econ Geol* 106:667–686.

Ushikubo, T., Williford, K.H., Farquhar, J., Johnston, D.T., Van Kranendonk, M.J., and Valley, J.W. (2014) Development of *in situ* sulfur four-isotope analysis with multiple Faraday cup detectors by SIMS and application to pyrite grains in a Paleoproterozoic glaciogenic sandstone. *Chem Geol* 383:86–99.

Valley, J.W. and Kita, N.T. (2009) *In situ* oxygen isotope geochemistry by ion microprobe. In *Secondary Ion Mass Spectrometry in the Earth Sciences: Gleaning the Big Picture from a Small Spot,* Mineralogical Association of Canada Short Course 41, edited by M. Fayeks, Mineralogical Association of Canada, Toronto, pp 19–63.

Wacey, D., Kilburn, M.R., Saunders, M., Cliff, J.B., Kong, C., Liu, A.G., Matthews, J.J., and Brasier, M.D. (2015) Uncovering framboidal pyrite biogenicity using nano-scale CN_{org} mapping. *Geology* 43:27–30.

Williams, G.E. and Schmidt, P.W. (1997) Paleomagnetism of the Paleoproterozoic Gowganda and Lorrain formations, Ontario: low paleolatitude for Huronian glaciation. *Earth Planet Sci Lett* 153:157–169.

Williford, K.H., Van Kranendonk, M.J., Ushikubo, T., Kozdon, R., and Valley, J.W. (2011) Constraining atmospheric oxygen and seawater sulfate concentrations during Paleoproterozoic glaciation: *in situ* sulfur three-isotope microanalysis of pyrite from the Turee Creek Group, Western Australia. *Geochim Cosmochim Acta* 75:5686–5705.

Williford, K.H., Ushikubo, T., Lepot, K., Kitajima, K., Hallmann, C., Spicuzza, M.J., Kozdon, R., Eigenbrode, J.L., Summons, R.E., and Valley, J.W. (2016) Carbon and sulfur isotopic signatures of ancient life and environment at the microbial scale: Neoarchean shales and carbonates. *Geobiology* 14:105–128.

Wing, B.A., Brabson, E., Farquhar, J., Kaufman, A.J., Rumble, D., III, and Bekker, A. (2002) $\Delta^{33}S$, $\delta^{34}S$ and $\delta^{13}C$ constraints on the Paleoproterozoic atmosphere during the earliest Huronian glaciation. *Goldschmidt Conference Abstracts*, A840.

Wing, B.A., Bekker, A., Brabson, L., Farquhar, J., Kaufman, A.J., and Rumble, D. (2004) Atmospheric chemistry of SO_2 during the earliest Huronian glaciation. *America Abstracts with Programs*, 36(5):339.

Wood, J. (1973) Stratigraphy and depositional environments of upper Huronian rocks of the Rawhide Lake-Flack Lake area, Ontario. In *Huronian Stratigraphy and Sedimentation,* Geological Association of Canada Special Paper 12, edited by G.M. Young, Marrais, Montreal, pp 73–95.

Xiao, S. (2014) Oxygen and early animal evolution. In *Treatise on Geochemistry,* 2nd ed., Vol. 6, The Atmosphere—History, edited by H.D. Holland and K.K. Turekians, Elsevier, Oxford, pp 231–250.

Xue, Y., Campbell, I., Ireland, T.R., Holden, P., and Armstrong, R. (2013) No mass-independent sulfur isotope fractionation in auriferous fluids supports a magmatic origin for Archean gold deposits. *Geology* 41:791–794.

Young, G.M. (1991) *Stratigraphy, Sedimentology and Tectonic Setting of the Huronian Supergroup,* Field Trip B5 Guidebook, Geological Association of Canada, Mineralogical Association of Canada, Society of Economic Geologists, Joint Annual Meeting Toronto '91, Toronto, Ontario.

Young, G.M. (2002) Stratigraphic and tectonic settings of Proterozoic glaciogenic rocks and banded iron-formations: relevance to the snowball Earth debate. *J Afr Earth Sci* 35:451–466.

Young, G.M., Long, D.G.F., Fedo, C.M., and Nesbitt, H.W. (2001) Paleoproterozoic Huronian basin: product of a Wilson cycle punctuated by glaciations and a meteorite impact. *Sedimentary Geology* 141–142:233–254.

Zhelezinskaia, I., Kaufman, A.J., Farquhar, J., and Cliff, J. (2014) Large sulfur isotope fractionations associated with Neoarchean microbial sulfate reduction. *Science* 346:742–744.

Zhou, L., McKenna, C.A., Long, D.G.F., and Kamber, B.S. (2017) LA-ICP-MS elemental mapping of pyrite: an application to the Palaeoproterozoic atmosphere. *Precambrian Res* 297:33–55.

Address correspondence to:
Huan Cui
NASA Astrobiology Institute
Department of Geoscience
University of Wisconsin–Madison
1215 W. Dayton St.
Madison, WI 53706, USA

E-mail: Huan.Cui@wisc.edu

Submitted 3 August 2017
Accepted 29 November 2017

Abbreviations Used

BSE = back-scattered electrons
EDS = energy-dispersive spectrometry
EPMA = electron-probe microanalysis
GOE = Great Oxidation Event
MDF = mass-dependent fractionation
MIF = mass-independent fractionation
SEM = scanning electron microscope
SIMS = secondary ion mass spectrometer
VCDT = Vienna Canyon Diablo Troilite

Appendices can be found with online Supplementary Material.

Appendix 1: Time-series SIMS data and equations used for SIMS data correction.

Appendix 2: Integrated BSE, SE images and SIMS data for the Kerr–McGee drill core 150–4.

Appendix 3: Integrated BSE, SE images and SIMS data for the Kerr–McGee drill core 156–1.

Appendix 4: Data table of the S four-isotopes analyzed by SIMS.

Appendix 5: Data table of the elemental concentrations analyzed by EPMA.